DISCLAIMER FOR FRONT PAGE OF MATERIALS TO BE MADE AVAILABLE VIA ETI INTERNET SITE

1. "Save to the extent set out in paragraph 2 below, this document and its contents are made available to you via the ETI's Internet Site "as is" without any representations, conditions, warranties or other assurance of any kind. The ETI and the authors, together with their employees, directors, servants or agents exclude to the maximum extent permissible by law all representations, warranties, conditions or other assurance whatsoever (whether express or implied) regarding the use of this document or its content including any warranties of title, merchantability, accuracy, completeness, non-infringement or that the document or its contents are of satisfactory or any particular quality or fit for any particular purpose. Any person accessing this document and using it or any of its contents accepts all risk in doing so.

2. Notwithstanding any statement to the contrary contained on the face of this document, the ETI confirms that the authors of the document have consented to its publication by the ETI."

Project	ReDAPT
Deliverable	MD1.4
Authors	I Afgan, U Ahmed, DD Apsley, T Stallard, PK Stansby
Circulation	University of Manchester, EDF
Date	20 October 2014
Version	1.3

CFD Simulations of a Full-Scale Tidal Stream Turbine: Comparison Between Large-Eddy Simulations and Field Measurements

by

I Afgan, U Ahmed, DD Apsley[1], T Stallard, PK Stansby
School of MACE
University of Manchester

---

[1] Corresponding Author

EXECUTIVE SUMMARY

This document represents deliverable MD1.4 and describes the application of EdF's open-source CFD solver *Code_Saturne* to large-eddy simulations (LES) of a full-scale tidal-stream turbine (TST). All simulations were performed with realistic approach-flow mean-velocity profiles. The objective of the work was to supplement this with realistic approach-flow turbulence and to extract frequency spectra of the fluctuating loads.

LES was conducted with both zero inlet turbulence and with a fluctuating velocity field synthesised from the stress profiles and length scales generated by a fully-developed channel-flow simulation. Turbulence profiles were further scaled to represent field measurements more accurately. The simulations follow on from Reynolds-averaged Navier-Stokes (RANS) computations reported earlier in MD1.5, but allow a more comprehensive evaluation of fluctuating loads on the turbine.

The main achievements are:
● full LES (up to 17.6 M cells) of the 1MW Alstom turbine at fixed rotation rate, including effects of turbulence and mean-flow velocity shear with realistic mean and turbulent velocity profiles from the EMEC test site;
● comparison of turbine loads, including time variation and spectra of blade bending moments, with measurements from the 1 MW Alstom turbine during operation at EMEC;
● simulations with three different turbulence characteristics and with two different approach-flow speeds to inform changes in behaviour during tidal cycles.

The primary findings of this report are as follows.
● LES is substantially more sensitive to spatial discretisation and gradient-reconstruction algorithms than RANS; in particular, it places stringent requirements on mesh quality (notably skewness), careful meshing near sliding interfaces (to ensure that ghost nodes lie wherever possible within the set of cells abutting the interface), better gradient reconstruction (to compute more accurate advective fluxes), centred differencing (for accuracy and to conserve energy) and smaller time steps (for stability).
● Mean power coefficients predicted by LES with inlet turbulence compare favourably with those measured at the EMEC test site, provided that the hub-height reference velocity is that immediately upstream of the turbine (say, one diameter upstream) and not on the inlet plane; this is because of flow development upstream of the turbine associated with the inlet turbulence prescribed by synthetic eddy modelling (SEM).
● If significant inlet turbulence levels are prescribed, velocity-profile development occurs between inlet plane and turbine. It is unclear whether this is an intrinsic fault of SEM (which can only provide statistically-correct first and second moments of a fluctuating velocity field) or the fact that statistics were supplied from a channel-flow simulation at much lower Reynolds number (the computing requirements for higher-Reynolds-number flow at comparable resolution are impractical).
● Intra-cycle variations of blade loading occur because of approach-flow velocity shear, interaction with the support tower, blade-generated turbulence and approach-flow turbulence. Only an eddy-resolving method such as LES provides any practical means of modelling the last two of these.
● Inflow turbulence makes little difference to mean blade bending moments or mean power, but greatly increases fluctuations in load and the influence of the support tower during a rotation.
● Power coefficients and blade bending moments (mean, phase-averaged and spectra) have been compared with field data. Realistic inflow turbulence is necessary to reproduce the spectrum of fluctuations in loads that are observed in experimental data. The vertical profiles of Reynolds stresses and length scales necessary to use SEM come from detailed channel-flow calculations (at a lower Reynolds number). We have investigated further scaling of these to match the Reynolds stresses and streamwise length scales measured at the EMEC site.

As this is the final Report of the series, a summary of the work undertaken earlier in the project is given as an Appendix.

CONTENTS

Nomenclature

A	turbine swept area
a_{ij}	Lund coefficients (Section 2.4)
C	a constant in a sub-grid-scale LES model
C_M	moment coefficient
C_P	power coefficient
c_p	pressure coefficient
C_s	Smagorinsky constant; part of a particular sub-grid-scale LES model
C_T	thrust coefficient
D	turbine diameter
$\hat{\mathbf{e}}$	unit vector
$\mathbf{F}$	force
f	Van Driest damping coefficient (Section 2.1)
	or
	shape function in the SEM model (Section 2.4)
	or
	frequency (Section 4.2)
f_0	main rotation frequency in time-varying loads
$f_{\max}$	maximum resolvable (Nyquist) frequency
h	channel depth
k	turbulent kinetic energy
L, L_x, L_y, L_z	
	length scales in the SEM model (Section 2.4)
L_{ij}	tensors related to products of fluctuating velocities (defined in Section 2.1)
$l_{ij}(x_\alpha)$	integral length scales in direction x_α
$\mathbf{M}$	moment of force
M_{ij}	tensor related to products of fluctuating velocities (defined in Section 2.1)
N	number of eddies in the SEM model
p	pressure

Q excess of rotational over shear strains (defined in Section 3.5)

R turbine radius

$\mathbf{r}$ displacement vector

r local radial distance from the turbine rotor axis

Re   Reynolds number

Re_τ Reynolds number based on friction velocity u_τ and channel depth h

R_{ij} correlation coefficient

$\|\mathbf{S}\|$ norm of the rate-of-strain tensor (defined in Section 2.1)

S_{ij} rate-of-strain tensor (defined in Section 2.1)

t time

T_0 period of one turbine revolution

$\mathbf{u}$ or (u_i) or (u_1, u_2, u_3) or (u, v, w)
     velocity vector

(u_i') fluctuating part of the velocity vector

U_A rotor-area-averaged mean velocity in the approach flow

U_b bulk (i.e. depth-averaged) mean velocity in the approach flow

U_{hub} hub-height mean velocity in the approach flow

U_0 reference velocity used to define dimensionless coefficients (tip-speed ratio, power coefficient etc); in this report we use the approach-flow mean velocity at hub-height: $U_0 = U_b$.

u_τ friction velocity, defined by $\sqrt{\tau_w / \rho}$

u^+ dimensionless velocity in wall units; defined by (*near-wall velocity*) / u_τ

V volume

(x_i) or (x_1, x_2, x_3) or (x, y, z)
     cartesian coordinates (z usually vertical)

y_n shortest distance to a wall (wall-normal: not necessarily in the y direction)

y^+ dimensionless distance (of a node) from a wall; given by $y^+ = (wall\ distance) \times u_\tau / \nu$

Greek symbols

Δ   "filter width" in an LES model: a typical length that can be resolved with a given mesh

ε_j^e normalised random numbers used to synthesise turbulent eddies (Section 2.4)

θ   angle

κ   Von Kármán's constant (≈ 0.41) in the universal near-wall velocity profile (Section 2.3)

ϕ   generic transported variable in the flow

μ   dynamic viscosity

μ_{SGS} sub-grid-scale viscosity in an LES model

ρ   density

τ_w wall shear stress

ν   kinematic viscosity ($= \mu / \rho$)

Ω   rotation rate

ω   specific dissipation (a variable in the k-ω turbulence model)

Abbreviations and Key Descriptions

ALE   arbitrary Lagrangian-Eulerian: a CFD approach on a moving mesh where the user specifies the mesh movement.

CFD   computational fluid dynamics

EMEC   European Marine Energy Centre (http://www.emec.org.uk/)

EW   edge-wise: about a perpendicular to the chord line in an aerofoil section.

FW   flap-wise: about the chord line of an aerofoil section.

LES   large-eddy simulation: the level of simulation that tries to compute all the time-dependent fluid flows that can be resolved on a computational mesh; a *sub-grid-scale model* is required to simulate the effect of eddies that are smaller than the mesh cells and hence can't be resolved.

RANS   Reynolds-averaged Navier-Stokes: the level of simulation that tries to compute the "average" (usually a time-, probability- or phase-average) behaviour; a *turbulence model* is required to simulate the effect of turbulent fluctuations that aren't resolved.

SEM   synthetic eddy modelling: a technique for supplying a statistically-correct fluctuating turbulence inlet field for large-eddy simulation.

SST   shear-stress transport; usually used as k-ω SST, a particular RANS turbulence closure.

TSR   tip-speed ratio: ratio of speed of a rotating blade tip (ΩR) to approach-flow velocity (U_0); a subscript b is used to denote a similar quantity, but normalised with the bulk velocity U_b.

TST   tidal stream turbine.

1. INTRODUCTION

1.1 Scope of this Document

This report explains the work undertaken to complete milestone MD1.4; specifically:
- LES simulations of the Alstom 1 MW turbine at a prescribed rotation rate and pitch angle, including realistic inflow mean-velocity and turbulence profiles;
- comparison with measured load data (including spectra) for time windows matching the flow conditions of the simulation.

1.2 Specific Tasks Associated With This Project

The specific milestones for the CFD work on the ReDAPT project are as follows. Major items in this report are in bold.

MD1.1	Ideal turbine geometry. Imposed rotation of a single cylindrical mesh (Coriolis forces or ALE). RANS turbulence. No waves. Report to identify development necessary for sliding mesh.
MD1.2	Ideal turbine geometry. Rotation via sliding mesh (including a description of the method). RANS and LES turbulence. Presentation of formulation and assumption of model and first assessment of the influence of turbulence model and characteristics on transient loads.
MD1.3	Alstom 1 MW turbine and structure geometry. Rotation imposed via new sliding-mesh method. RANS only simulation. Waves (modelled by ALE) and assessment of the influence of waves on time-varying loads and output.
MD1.5	Establishment of representative mean-velocity profiles at a tidal stream site, based on field measurements. RANS simulations of the effect of shear profiles of velocity and (isotropic) turbulence on unsteady loading of 1 MW turbine. Structure of anisotropic turbulence established by LES simulations of fully-developed (periodic) channel flow and represented by Synthetic Eddy Model (SEM) inflow to a finite-length channel. Summary of the inflow parameters required to represent EMEC flow in the LES simulations of MD1.4.
MD1.4 (This Report)	**LES simulations with the Alstom 1 MW turbine and structure geometry, using realistic mean velocity and synthetic eddy turbulence at inflow. Rotation imposed via sliding-mesh method. Assessment of the effects of turbulence on transient loads and power output. Comparison with field data.**

1.3 ETI Acceptance Criteria For MD1.4

The original acceptance criteria specified 3-d CFD simulations performed with:
– rotating blades with imposed velocity and an internal sliding-mesh boundary;
– detailed geometry and mast;
– turbulence via LES;
– waves.

Validation would be by comparison with data from literature, and, if available, with ReDAPT data. Acceptability of the model could be related to its ability to reproduce trends and orders of magnitude on the following results: loads, velocity fields and turbulence in the near wake. Simulations were to be performed with the full model, taking into account turbulence and wave effects. Mean current speeds provided by MD5.2 would be considered for boundary conditions. The MD1.4 report would present detailed formulations and assumptions of the model, the results of validation, and the assessment of the effects of turbulence and waves on transient loads, downstream wake structures and power output.

The scope of this deliverable has been adjusted over the duration of the ReDAPT project. This is due to the type and extent of data collected and due to the importance of specific operating conditions. Key changes concern waves, the mean current data employed and the extent of analysis of the wake.

Waves
This deliverable does not address loading due to waves. Simulation of waves and their influence on loads was studied with a RANS CFD method in MD1.3. Blade loading due to waves is greatly influenced by blade pitch. This is not simulated in the CFD model developed throughout MD1 and so direct comparison between CFD and full-scale measurements would not be informative. This, combined with limitations on type and extent of wave data available from the EMEC site, led to this report being confined to the influence of the flow profile and turbulence on blade loading.

Mean current speeds
Numerical modelling and analysis of depth profiles conducted in MD5.2 showed that the depth profile of velocity and turbulence at the deployment site varied considerably during a tide. The detailed measurement campaigns conducted during MD3 have provided improved insight into these flow profiles and the turbulence characteristics. The onset flows studied in this deliverable are thus informed by MD5.2 and the measurements and analysis of MD3.

Wakes
Due to the high computational time required for LES simulations and the much greater availability of loading data than wake velocity measurements, the focus of this deliverable is on turbine loading rather than the characteristics of the wake.

1.4 Staff on the Project

There have been a number of staff changes during the ReDAPT project. The current post-doctoral researcher employed on this project is Dr Umair Ahmed. Earlier major contributions came from: Dr James McNaughton, who did much *Code_Saturne* code development as well as creating the geometric model and mesh for this and an earlier turbine; Yacine Addad; Stefano Rolfo, who tested the synthetic eddy modelling procedures that provide the turbulence input field for the LES and performed the accompanying channel-flow simulations; Dr Imran Afgan (now on the lecturing staff), who undertook many LES calculations on an earlier generic turbine.

The academic staff associated with the project are Prof. Peter Stansby (Principal Investigator), Dr Imran Afgan, Dr David Apsley and Dr Tim Stallard.

2. MODELLING

2.1 LES Constitutive Relation

The continuity and momentum equations for the spatially-filtered (i.e. resolved on the current mesh) velocity components (u_i) are, in conservative form,

$$\frac{\partial u_j}{\partial x_j} = 0$$

$$\frac{\partial}{\partial t}(\rho u_i) + \frac{\partial}{\partial x_j}(\rho u_i u_j) = -\frac{\partial p}{\partial x_i} + \frac{\partial}{\partial x_j}\left[(\mu + \mu_{SGS})(\frac{\partial u_i}{\partial x_j} + \frac{\partial u_j}{\partial x_i})\right]$$

The subgrid-scale eddy viscosity is given by:

$$\frac{\mu_{SGS}}{\rho} = C\Delta^2\|\mathbf{S}\|f \tag{1}$$

where

$$\|\mathbf{S}\| = \sqrt{2S_{ij}S_{ij}}, \qquad S_{ij} = \frac{1}{2}\left(\frac{\partial u_i}{\partial x_j} + \frac{\partial u_i}{\partial x_j}\right)$$

and, where applied (see below), the Van Driest low-Re damping function f is reduced from 1 to

$$f = 1 - e^{-y^+/26}$$

In the standard Smagorinsky model,

$$C = C_s^2$$

Code_Saturne has a default value $C_s = 0.065$ and assumes a filter width (nominally, the minimum resolved-eddy size) of

$$\Delta = 2(cell\ volume)^{1/3}$$

The Van Driest damping function is invoked with the standard Smagorinsky model.

In the present work a version of the more advanced dynamic subgrid-scale model of Germano et al. (1991), as modified by the popular least-squares formulation of Lilly (1992), was employed. The essence of the model is that the subgrid-scale eddy-viscosity relationship (in particular the local value of C) should be independent of the size of the filter (i.e. the fineness of the mesh), provided that this is sufficiently small. The result of minimising the squared difference between unresolved stress and strain using equation (1) on two different scales Δ and $\hat{\Delta}$ is that C is not spatially or temporally constant, but given locally by

$$C = \frac{L_{ij}M_{ij}}{M_{ij}M_{ij}}$$

where

$$L_{ij} = -(< u_i u_j > - < u_i >< u_j >), \qquad M_{ij} = 2\hat{\Delta}^2\|< \mathbf{S} >\|< S_{ij} > -2\Delta^2 <\|\mathbf{S}\|S_{ij} >$$

and $<>$ denotes a spatial average of the Δ-resolved velocities (i.e. those in the computation) over the larger filter width $\hat{\Delta}$. In the *Code_Saturne* implementation the larger filter consists of the "extended neighbourhood" of a cell; i.e. over all cells sharing a common vertex. The Van Driest damping function is not employed with the dynamic subgrid model, which is intended to sense the flattening of eddies near a boundary automatically.

Note that Lilly (1992) allows, in principle, for "backscatter"; i.e. $C < 0$. This amounts to a negative diffusivity and causes numerical problems. It is not permitted in the present implementation, where C is constrained to lie between 0 and 0.13^2. Lilly's paper uses a definition of M_{ij} half that in this Report.

2.2 Discretisation

Except in the early stages of a simulation (where first-order upwind differencing was used to maintain stability during initial transients and to permit a faster approach to developed flow), the values of transported scalars on cell faces were determined by central differencing, except where the advection scheme reverted locally to upwind differencing when a simple slope test detected non-monotonicity; i.e. if the scalar product of gradients either side of a cell face was negative.

Results for LES calculations were found to be particularly sensitive to the method of gradient reconstruction (i.e. determination of cell-averaged gradients from values at surrounding nodes) which is needed for various parts of flux-discretisation and turbulence models. Initial calculations were done by the least-squares approach, which is an explicit procedure leading to the gradient $(\nabla\phi)_I$ of a general transported variable ϕ for cell I being the vector which minimises the sum of squared errors between

$$\phi_J \qquad \text{and} \qquad \phi_I + \mathbf{r}_{IJ} \bullet (\nabla\phi)_I$$

taken over all nearest neighbouring cell-centre nodes J. This may be biased if there are, for example, more "nearest neighbours" on one side of a cell than another (e.g. near a boundary). A more accurate approach is that based on Gauss's Theorem relating volume integrals of derivatives (or, as here, cell-averaged derivatives) with surface integrals:

$$(\nabla\phi)_{av} = \frac{1}{V}\int_{\partial V} \phi \ d\mathbf{A}$$

where V is the volume of a cell and ∂V its bounding surface. Since ϕ on a cell face depends on the gradient $\nabla\phi$ at neighbouring cells this has to be obtained iteratively, with the least-squares approach as a first guess. This is referred to as "iterative reconstruction" in the *Code_Saturne* Theory Manual. Load calculations suggest that this technique improves flux accuracy and power coefficients and it was used for the simulations presented here. To use this form of gradient it is vital to ensure proper convergence of the ALE/sliding-mesh iteration within each timestep.

Because of numerical stability and LES implementation issues in *Code_Saturne*, first-order, fully-explicit timestepping was used throughout, with timestep 2.5×10^{-4} s during the main averaging phase. It was found useful to develop the flow quickly by using upwind differencing and a much higher timestep (0.05 s) for the first pass-through, before switching to the smaller timestep for accurate statistics. A fixed number of iterations (NTERUP = 5) was used for the inner iteration (pressure correction and sliding mesh) because no other convergence criterion is presently available in *Code_Saturne*. The number adopted was a conservative one, based on a series of numerical trials, and is slightly larger than the value of 3 found to be required for RANS calculations (McNaughton, 2013).

2.3 Boundary Conditions

All transport variables were prescribed at inlet. Several cases were considered (Section 3). For comparison with earlier RANS results a basic LES (Case 1) was performed with zero inlet turbulence and mean velocity following the monotonic "flood" profile used in earlier studies and shown in Figure 1. (Note that the experimental data shown on the left of the figure includes some measurements taken in the wake of a support structure and turbine.) The remaining LES simulations used inlet fluctuations imposed via SEM and based on turbulent stresses and lengthscales determined in a separate channel-flow simulation (see Section 2.4). For SEM simulations the mean-velocity profile was that of the channel-flow simulation, scaled to give a bulk velocity of 1.8 m s^{-1}. A single simulation (Case 4) with higher bulk velocity of 2.6 m s^{-1} (but same tip-speed ratio), was also performed.

A constant-pressure outlet condition was used, together with symmetry planes on side-walls and bottom and top boundaries. As agreed in discussion with the ReDAPT partners and summarised in earlier reports, no attempt was made to simulate waves on the free surface.
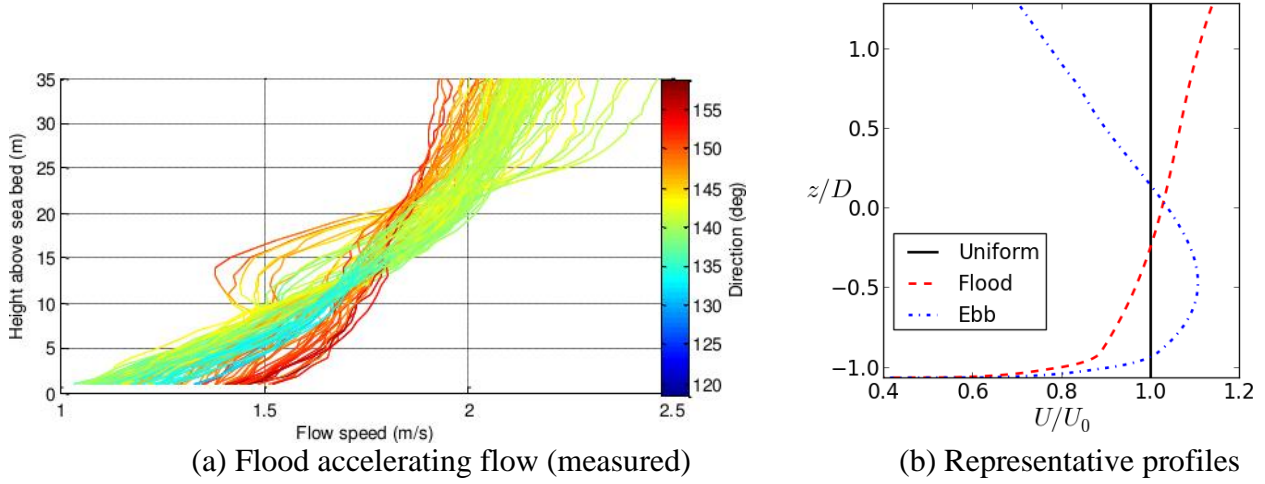
(a) Flood accelerating flow (measured)   (b) Representative profiles

Figure 1. Inflow mean-velocity profiles.

At the high Reynolds numbers associated with the full-scale turbine it is prohibitively expensive to undertake wall-resolved LES simulations and so a wall-function approach was applied at all solid boundaries (turbine, support tower and ground). The standard *Code_Saturne* wall-function approach uses a continuous (but slope-discontinuous) assumed near-wall velocity profile in wall units:

$$u^+ = \begin{cases} y^+ & \text{if } y^+ \leq 10.88 \\ \dfrac{1}{\kappa}\ln y^+ + 5.2 & \text{if } y^+ \geq 10.88 \end{cases}$$

where

$$u^+ = \frac{u}{u_\tau}, \qquad y^+ = \frac{u_\tau y_n}{\nu}$$

This provides the local friction velocity u_τ (and hence the wall shear stress) from the near-wall values of tangential velocity u and wall-normal distance y_n. Since the linear form coincides with that used to discretise velocity gradients, wall functions are effectively switched off if $y^+ \leq 10.88$.

2.4 Synthetic-Eddy Modelling (SEM) For Inflow Turbulence

Synthetic eddy modelling supplies an LES calculation with a fluctuating inlet velocity field with the intended statistical distribution of Reynolds stresses and turbulent length scales. Following simulations of fully-developed channel flow (reported in MD1.5) the SEM variant used in the current work is based on that of Jarrin et al. (2009).

Fluctuating velocities are generated from eddies advected through a virtual box (volume V_B) containing the nominal inlet plane. As each eddy leaves the box another eddy is generated at a random location on the box inlet plane. The velocity fluctuations are given by

$$u_i'(\mathbf{x}) = \frac{1}{\sqrt{N}}\sum_{e=1}^{N} a_{ij}\varepsilon_j^e f_L(\mathbf{r}_e)$$

where:

$\mathbf{r}_e = \mathbf{x} - \mathbf{x}_e$ is the displacement relative to the centre $\mathbf{x}_e$ of eddy e;
N is the number of eddies in the box;
a_{ij} are the Lund coefficients (Cholesky decomposition $\mathbf{a}^T\mathbf{a}$ of symmetric tensor $\overline{u_i u_j}$);
ε_j^e are a set of random numbers with mean 0 and variance 1 for eddy e;

$$f_L(\mathbf{x}) = \sqrt{\frac{V_B}{L^3}} f(\frac{x}{L_x}) f(\frac{y}{L_y}) f(\frac{z}{L_z})$$

L_x, L_y and L_z are eddy length scales, with $L = \frac{1}{3}(L_x + L_y + L_z)$

f is a shape function, here taken as $f(\xi) = \max(\sqrt{\frac{3}{2}}(1 - |\xi|), 0)$

The main inputs to SEM are the vertical profiles of length scales L_x, L_y and L_z and stresses $\overline{u_i u_j}$. For this work they have been derived from the fully-developed channel-flow LES described in MD1.5 at $\mathrm{Re}_\tau = 9300$, scaled to the desired bulk velocity U_b and depth h; i.e.

$$\overline{u_i u_j} = \left(\frac{U_b}{U_{b,ref}}\right)^2 (\overline{u_i u_j})_{ref}$$

$$L = \left(\frac{h}{h_{ref}}\right) L_{ref}$$

where "*ref*" denotes the channel-flow value. (The original channel-flow calculation was non-dimensionalised with respect to friction velocity u_τ and channel depth h. In these units, $U_b/u_\tau = 22.4$.)

Length scales L_x, L_y, L_z in SEM are different for each of the three fluctuating velocity components and are based on the integral length scales measuring correlation in each direction. Specifically, we take

$$L_\alpha (\textit{for velocity component } u_\beta) = l_{\beta\beta}(x_\alpha)$$

For example, for the u_2' component,

$$L_x = l_{22}(x)$$
$$L_y = l_{22}(y)$$
$$L_z = l_{22}(z)$$

The integral length scales are determined from two-point correlations by

$$l_{\beta\beta}(x_\alpha) = \frac{1}{R_{\beta\beta}(0)} \int_0^\infty R_{\beta\beta}(r\hat{\mathbf{e}}_\alpha) \ dr$$

where

$$R_{ij}(\mathbf{r}) = <u_i(\mathbf{x},t)u_j(\mathbf{x}+\mathbf{r},t)>$$

and $\hat{\mathbf{e}}_\alpha$ denotes the unit vector in the x_α direction. (The dependence of R_{ij} on position $\mathbf{x}$ has been omitted for clarity, but all the correlations are functions of height z). Hence, 9 integral length scales are required (l_{11}, l_{22}, l_{33} in each of the x, y, z directions) at each height z.

The mean velocity, Reynolds stresses and length scales determined by fully-developed channel-flow simulations (at a lower Reynolds number, as reported in MD1.5) are shown in Figures 2, 3 and 4 respectively. Once scaled to the appropriate bulk velocity, the channel-flow mean-velocity profile (Figure 2) exhibits slightly greater shear across the turbine rotor than the flood profile. Of more interest is whether profiles of mean velocity, Reynolds stresses and length scales are similar to field measurements (see below). The main reason for using the channel-flow mean-velocity profile here is that it should be better at maintaining the specified turbulence profiles from inlet to rotor plane during a computation.

Figure 5 shows a typical instantaneous velocity field at inlet where SEM has been applied.
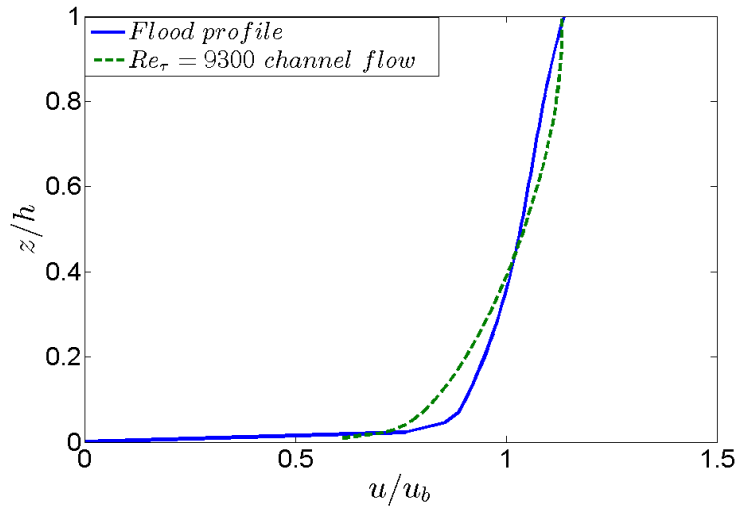
Figure 2. Mean-velocity profile from channel-flow simulation; comparison with the flood profile.
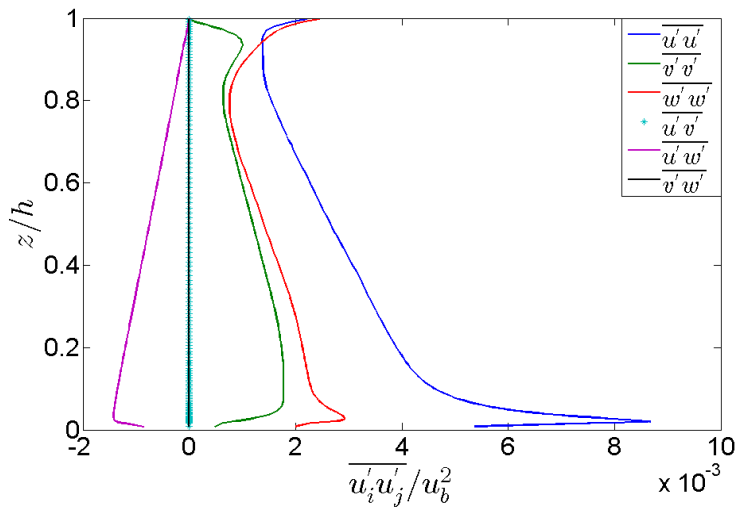

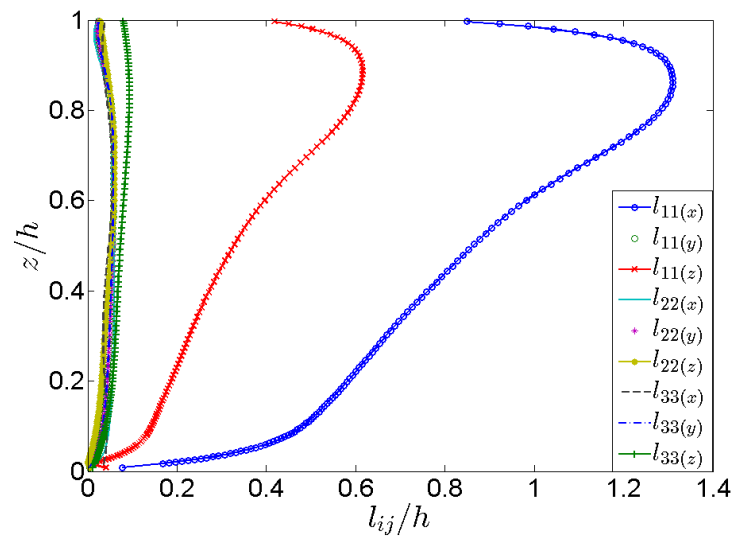**Figure 3.** Reynolds-stress profiles from the channel-flow simulation.

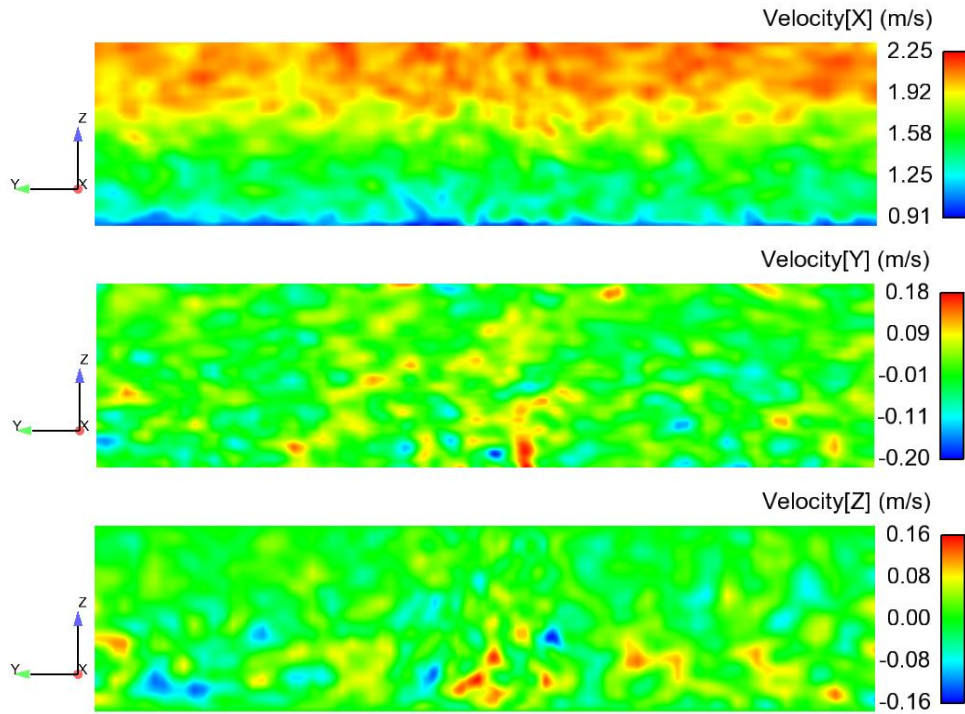**Figure 4.** Length-scale profiles from the channel-flow simulation.

Figure 5. Synthesised velocity field at inflow.

For the EMEC site and Alstom turbine, Figure 4 implies a streamwise length scale $l_{11}(x)$ at hub height ($z_{hub} / h = 0.45$) of about 34 m ($l_{11} / h = 0.8$). Extensive measurements of velocity upstream and adjacent to the turbine were obtained and analysed by the University of Edinburgh to determine these parameters for the flow incident to the turbine (documented in MD3 reports). Preliminary analysis of subsets of this data was reported by DNV-GL (MD6.2) and indicated an $l_{11}(x)$ length scale of around $30 - 35$ m for flow speeds of approximately 1.8 m s^{-1}. This would be in accord with the corresponding lengthscale in Figure 4. However, further analysis was conducted by the University of Edinburgh (to be reported in MD3.8) with a particular focus on determining these parameters for flow-speed bins of 0.2 m s^{-1} width centered around 1.8 m s^{-1} and 2.6 m s^{-1}. More than 160 samples of time-varying flow speeds were identified with average speed in the range $1.7 - 1.9$ m s^{-1} occurring during a flood tide and with threshold filters applied on the magnitude of flow acceleration and wave intensity during the sample. $l_{11}(x)$, $l_{22}(x)$ and $l_{33}(x)$ at mid-depth during a flood tide of 1.8 m s^{-1} were reported to be in the range $7 - 22$ m, $2 - 7$ m and $1 - 4$ m respectively; these are, typically, about half of those suggested by the channel-flow simulation. To examine the potential effect of this difference of length scales, two simulations were performed at flow speed 1.8 m s^{-1}: the first with length-scale profiles taken directly from the channel simulations and the second with the length scales halved (see Section 4).

Figure 6 indicates how closely the prescribed inlet velocity statistics match experimental data. Normalised field data from flow speeds in the ranges 1.8±0.1 m s^{-1} and 2.6±0.3 m s^{-1} is compared with that prescribed in SEM calculations (Cases 2 to 4). There is reasonable agreement over the range of heights swept by the rotor, but some difference near the bed.

Figure 7 seeks to establish how much computed flow development occurs between inlet and turbine (actually, a vertical line $2D$ upstream of the turbine or $3D$ downstream of the inlet) and whether this is influenced by the additional factoring of inlet length scales and (for the higher-speed case) Reynolds stresses to match field data. Data is, at present, averaged only over a single rotation, so that large-scale turbulent structures are clearly evident. Longer averaging times are clearly necessary; however, there

is some indication of flow development, with lower speeds near the bed and higher speeds near the surface, increasing the velocity shear as the computed turbulent flow approaches the turbine.
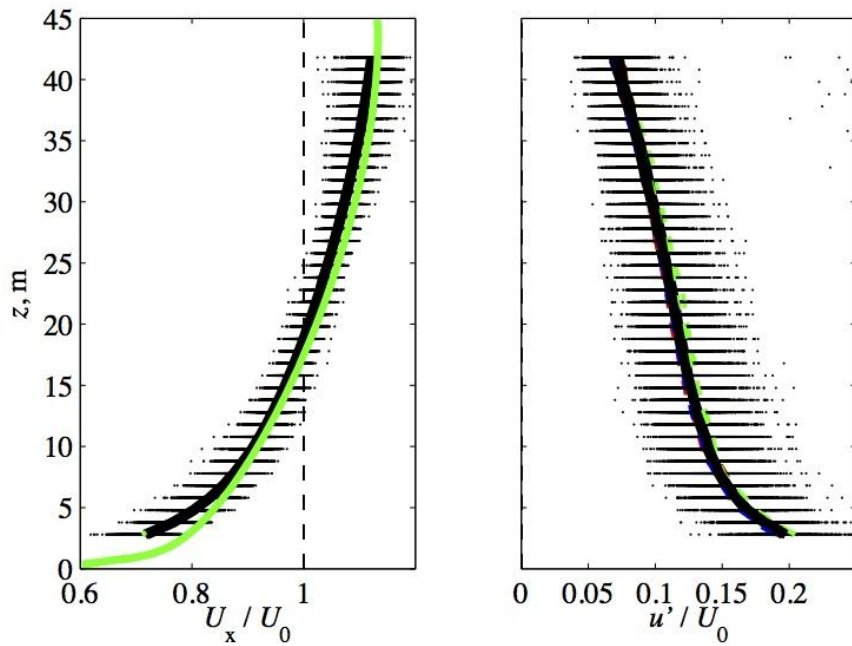

Figure 6. Comparison of prescribed mean and streamwise fluctuating velocity profiles with field data; green line - SEM prescription; black markers and line - experiment.
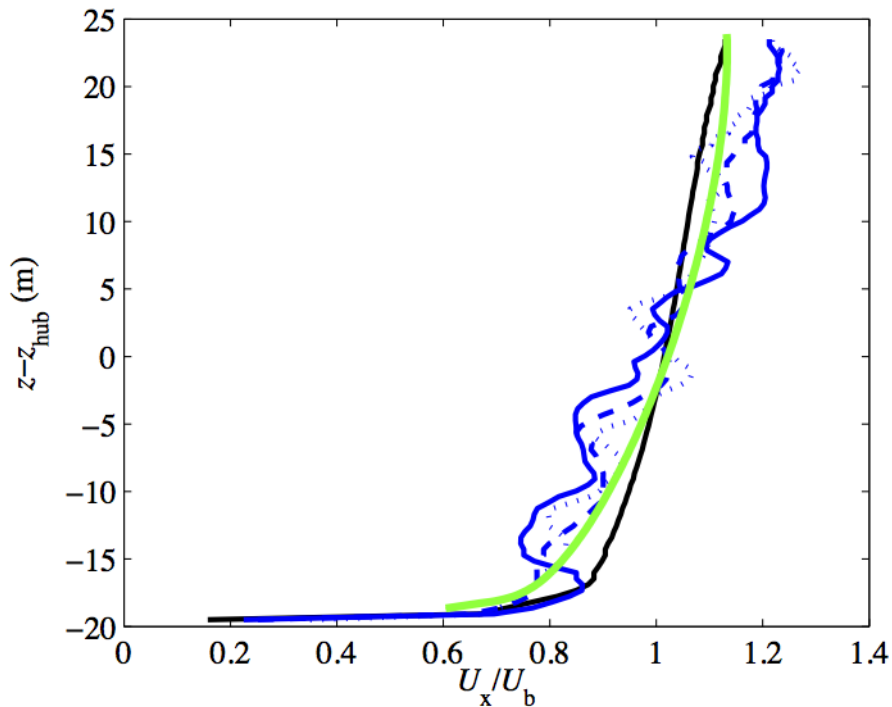

Figure 7. Streamwise velocity profiles; black - flood profile; green - inlet mean velocity prescribed for SEM; solid / dashed / dotted blue - profiles computed 2D upstream of rotor (averaged over one rotation) with inlet SEM prescribed by channel flow / channel flow with factored length scales / channel flow with factored length scales and Reynolds stresses.

3. SIMULATIONS

3.1 Model Geometry

Model geometry and meshing was largely developed for the previous report (MD1.5), but finer meshes have been developed in accordance with the requirements of LES. Model geometry was supplied as CAD files. Meshes were produced using ICEM, part of the ANSYS Fluent suite. The basic geometry and domain dimensions are shown in Figure 8. As shown in that figure, an inner cylindrical region of cells (containing the turbine rotor), rotates inside a stationary outer domain (which includes the turbine support tower). The two regions are connected by a sliding interface, the methodology and implementation of which has been reported earlier (MD1.2 and McNaughton et al., 2014).

The main geometric parameters were as follows:
  rotor diameter: $D = 18.296$ m;
  domain depth: $h = 43$ m ($= 2.350D$);
  hub height: $z_{hub} = 19.5$ m ($= 1.066D$ or $0.453h$);
  domain length: 90 m upstream and 180 m downstream of the rotor plane ($4.92D$ and $9.84D$).
In the computational model the coordinate origin is at the centre of the rotor and the inner rotating region has diameter 20 m.

We note that, for a nominal approach-flow speed of 1.8 m s^{-1} and tip-speed ratio (TSR) of 6 (precise values are given in Section 3.4), important timescales are:
  time for one blade rotation ≈ 5.2 s;
  time for onset flow to reach the rotor plane: ≈ 50 s;
  time for one domain pass-through: ≈ 150 s.
Note that, although simulations used slightly different approach-flow speeds (for example, the flood profile has bulk velocity 1.826 m s^{-1}, whilst the lower-speed SEM calculations fixed *bulk velocity as* precisely 1.8 m s^{-1}), differences are eliminated by presenting results in dimensionless form.

(a) View of the surface mesh　　　　　　　　　(b) Dimensions of the computational domain.
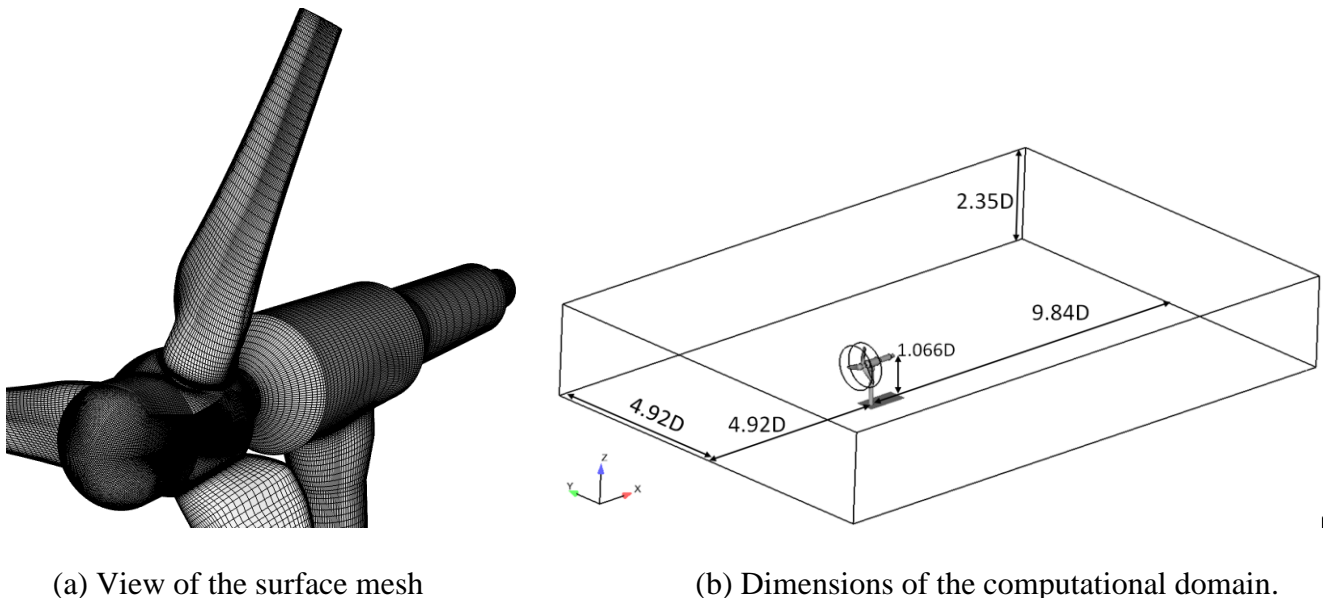
Figure 8. Overview of geometry and turbine mesh.

3.2 Computational Mesh

The mesh used for RANS simulations contained a number of very skew cells which caused numerical problems in LES. In addition, the large mismatch in radial depth of cells either side of the interface caused numerical instabilities and errors in the pressure field in LES calculations which were not observed with RANS simulations (probably due to the inherently stabilising turbulent viscosity associated with the latter). Considerable effort was expended in restructuring and refining the mesh to improve mesh quality. In addition, efforts were made to reduce y^+ values near blade tips. Some details of the mesh are shown in Figures 9 and 10. With hindsight, mesh quality would have been easier to control with a larger-diameter inner rotating region, but this was fixed at the time to allow for changes in surface height in the outer domain due to waves, a feature which was not ultimately pursued.

(a) Mesh used for previous RANS studies   (b) Revised mesh used in present study
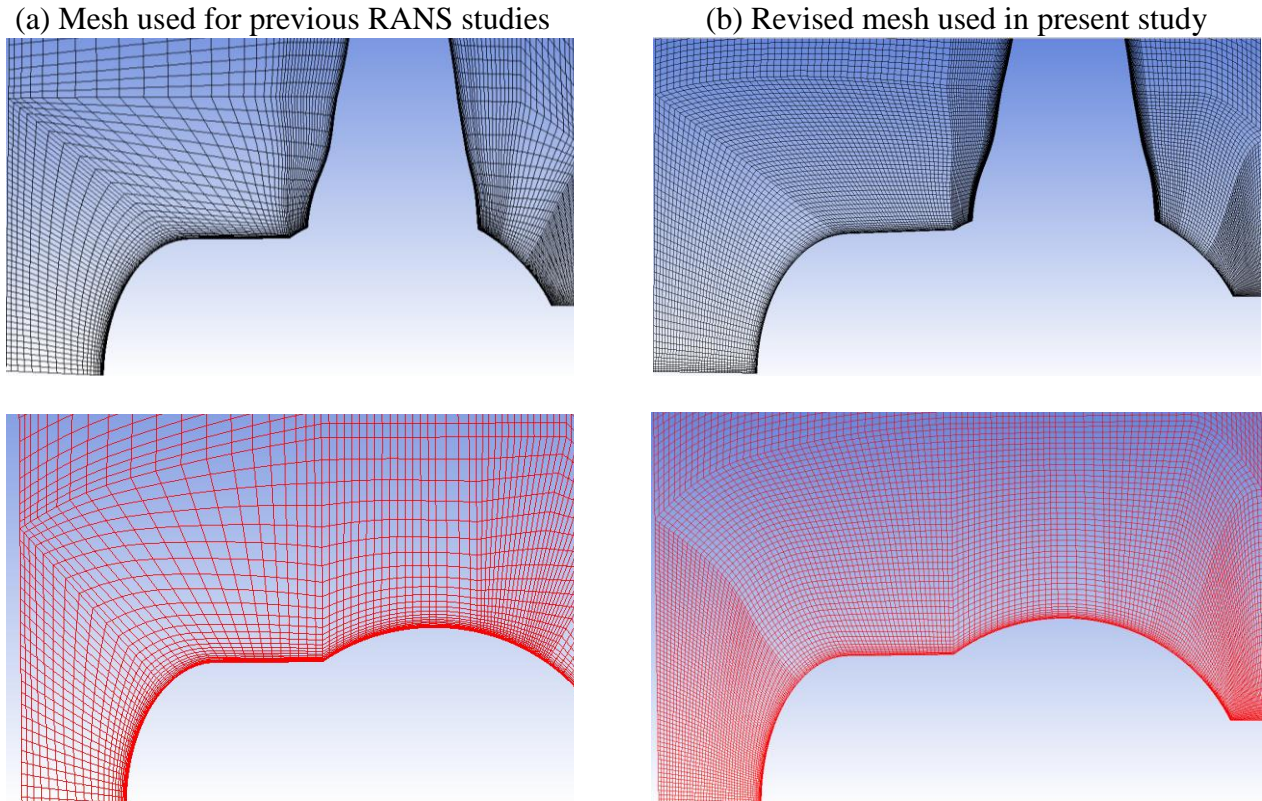
Figure 9. Mesh near the nacelle.
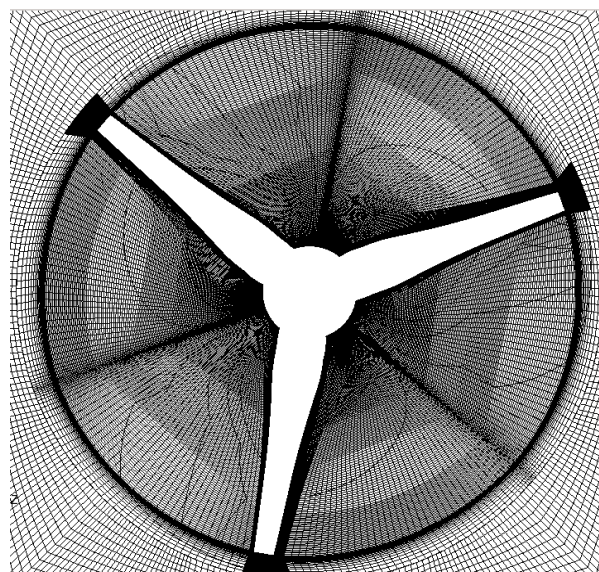
Figure 10. Mesh cross-section, showing the interface.

3.3 Non-Dimensional Parameters

The main performance-related parameters are defined below.

Tip-speed ratio:
$$\text{TSR} \equiv \frac{\Omega R}{U_0}$$

Thrust coefficient:
$$C_T = \frac{force_x}{\frac{1}{2}\rho U_0^2 A}$$

Power coefficient:
$$C_P = \frac{torque \times angular\ velocity}{\frac{1}{2}\rho U_0^3 A}$$

Here, A is the rotor swept area and U_0 is a suitable approach-flow reference velocity. For the latter, there are a number of possible candidates:

U_b bulk (i.e. water-column depth-averaged) mean velocity

U_{hub} mean velocity at hub height

U_A mean velocity averaged over the turbine swept area

and others (e.g. power-weighted: based on the average of U^3 over the turbine swept area). In order to compare directly with the available experimental data, in this report U_0 is taken as the hub-height velocity. In earlier reports we used U_b (because the height of the hub could potentially be a design variable, and also because the bulk velocity, being based on flow rate, doesn't change if there is upstream flow development). Because the rotation rates in the simulations were actually set by fixing tip-speed ratio using bulk velocity, we introduce a second tip-speed ratio:

$$\text{TSR}_b \equiv \frac{\Omega R}{U_b}$$

with the subscript b indicating use of the bulk velocity rather than hub-height velocity.

To allow users to translate to other velocity scales we have listed the relevant velocities and rotation rates in the table of cases in Section 3.4.

Also of interest to designers are blade bending moments, the coefficients of which are

$$C_M = \frac{moment}{\frac{1}{2}\rho U_0^3 A}$$

Two particular moment axes are considered: *flapwise* and *edgewise*. "Flapwise" refers to the moment of forces about the chord line. "Edgewise" refers to the moment of forces about an axis in the plane of the cross-section and perpendicular to the chord, in this case passing through the "pitch axis", which at both locations is 35% chord from the leading edge. Figure 11 defines the axes for these moments.
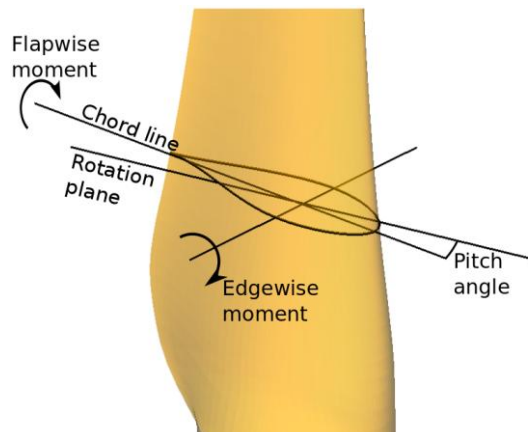

Figure 11. Definition of axes for blade bending moments.

Computationally, the bending moments may be computed by projecting the net moment of force about the reference point $\mathbf{r}_{ref}$ onto a unit vector in the direction of the relevant axis, $\hat{\mathbf{e}}_{axis}$:

$$M_{axis} = \hat{\mathbf{e}}_{axis} \bullet \sum (\mathbf{r} - \mathbf{r}_{ref}) \wedge \mathbf{F}$$

where $\mathbf{F}$ is the net surface force (pressure plus shear stress) on each cell face and the summation is over the blade surface at greater radius than the reference point.

3.4 Summary of Simulations Undertaken

Code_Saturne v2.06 was used for all simulations in this report. Calculations were undertaken on EdF's BlueGene Q supercomputer, using 4096 cores per simulation.

The following simulations were undertaken.

Case 1 employed the inlet "flood" profile of earlier reports for mean velocity, together with zero inlet turbulence. To compare directly with RANS, we fixed the rotation rate to give a tip-speed ratio of 6.0 when based on a nominal reference velocity of 1.8 m s^{-1}. The actual bulk and hub-height velocities are slightly larger than this, giving the TSR values in the table below.

Case 2 employed SEM to synthesise inlet turbulence, with mean-velocity and corresponding profiles of Reynolds stresses and length scales determined by LES channel-flow simulations (reported in MD1.5), scaled to give a channel depth $h = 43$ m and bulk velocity $U_b = 1.8$ m s^{-1}. The rotation rate was fixed by requiring TSR$_b = 5.2$ (based on experimental data for this flow speed). Comparison to Case 1 established the overall influence of a turbulent inflow, and the corresponding velocity depth profile, on unsteady loads.

Case 3 was as for Case 2, but with integral length scales halved, as suggested by experimental data from the EMEC site for this bulk velocity; (see Section 2.4). Comparison to Case 2 established the influence of turbulence length scale on unsteady loads.

Case 4 was as for Case 2, but with a higher bulk velocity, $U_b = 2.6$ m s^{-1}. (The rotation rate was increased to maintain the same TSR$_b = 5.2$.) Depth profiles of both Reynolds stresses and length scales input to the SEM calculation were factored by 1.8 and 0.5 respectively to match experimental measurements of Reynolds stresses and the streamwise length scale at mid-depth. Comparison with Case 2 and 3 established the influence of turbulence characteristics on unsteady loads. Comparison with experimental measurements of blade-root bending enabled evaluation of this approach for prediction of operational loads.

Case	Inlet mean velocity	Inlet turbulence	U_b (m s^{-1})	TSR$_b$	Ω (rad s^{-1})	U_{hub} (inlet) (m s^{-1})	U_{hub} (1D up.) (m s^{-1})	TSR
1	Flood profile	Zero	1.826	5.915	1.181	1.844	1.842	5.857
2	Channel flow	SEM based on channel flow	**1.8**	**5.2**	1.023	1.848	1.725	5.070
3	Channel flow	SEM based on channel flow, but: length scales $\times$ 0.5	**1.8**	**5.2**	1.023	1.848	1.741	5.070
4	Channel flow	SEM based on channel flow, but: length scales $\times$ 0.5, $\overline{u_i u_j} \times 1.8$	**2.6**	**5.2**	1.478	2.669	2.483	5.069

Values in **bold** in the table were **specified**; Ω was then computed from them. Case 1 was originally set up for a TSR of 6 with nominal reference velocity 1.8 m s^{-1}; actual bulk and hub-height velocities are slightly larger than this. For flows with inlet turbulence (simulated by SEM; cases 2–4) there is developing flow, which means that the hub-height mean velocity differs between the inlet plane and a plane one diameter upstream of the turbine rotor. This has a significant effect on load coefficients, as the hub-height velocity is used as the relevant scale – see Section 4.

3.5 Flow-Field Overview

Figure 12 shows the instantaneous velocity field from LES, comparing the zero turbulence inflow with that synthesised by SEM. The influence of the rotor is typically felt up to one diameter upstream. Note in all cases the well-defined wake of the rotor and the interaction with the support tower (and the ground). In the SEM calculations, flow structures are advected without significant dissipation from inlet to turbine rotor, but vortical structures shed from the blades are diffused more rapidly. Halving turbulent length scales creates smaller, better-defined vortical structures and, by increasing dissipation and reducing diffusion, leads to sharper vortical structures shed from turbine, nacelle and support.
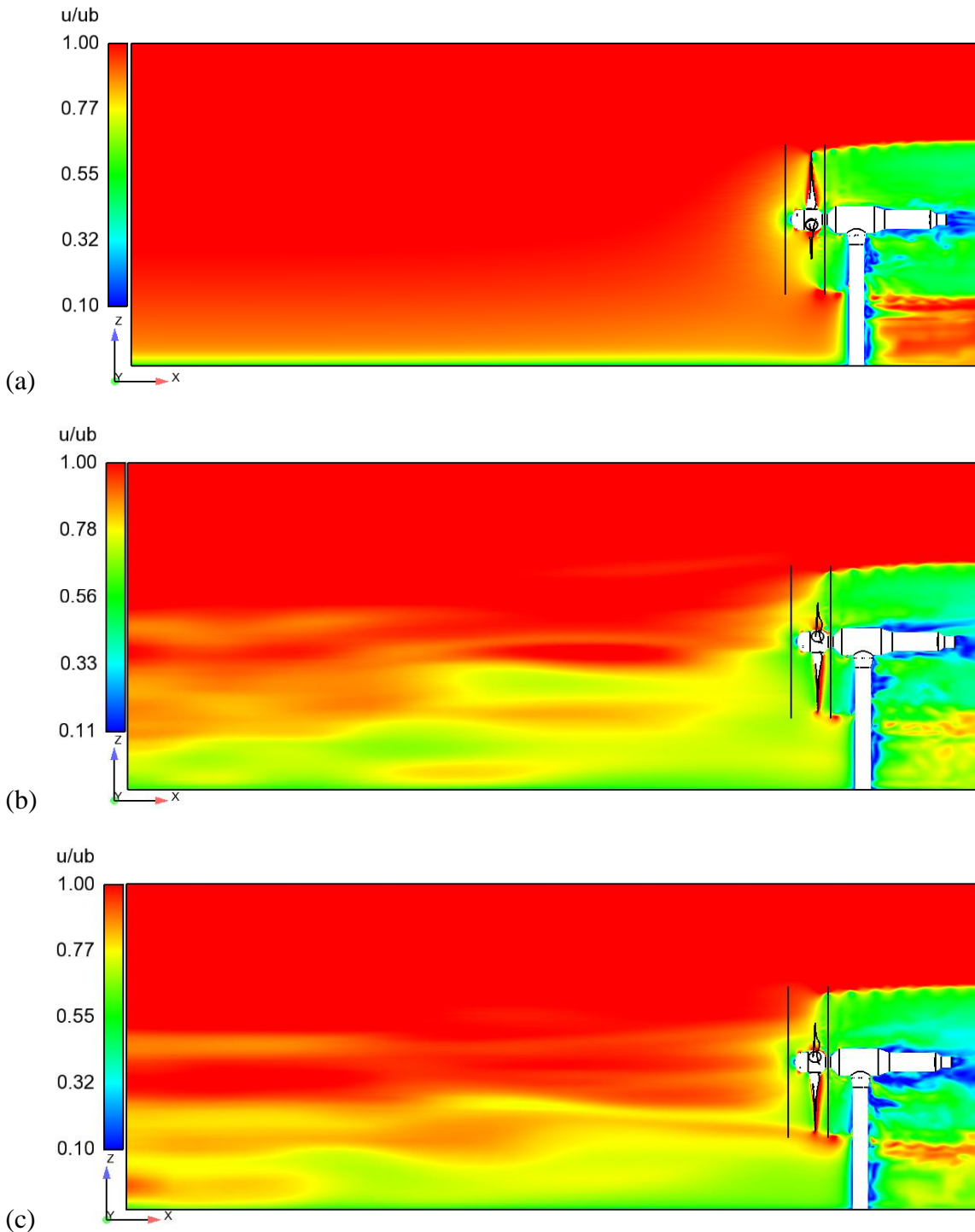
Figure 12. LES Velocity field: (a) no inlet turbulence, Case 1; (b) SEM turbulence at inflow, Case 2; (c) SEM turbulence with reduced lengthscales, Case 3.

A close-up view of the zero-turbulence simulation, is shown in Figure 13. Note that the wake does not spread significantly, whilst vortices shed from blade tips persist a considerable distance downstream. This has implications for the operation of turbines in arrays.
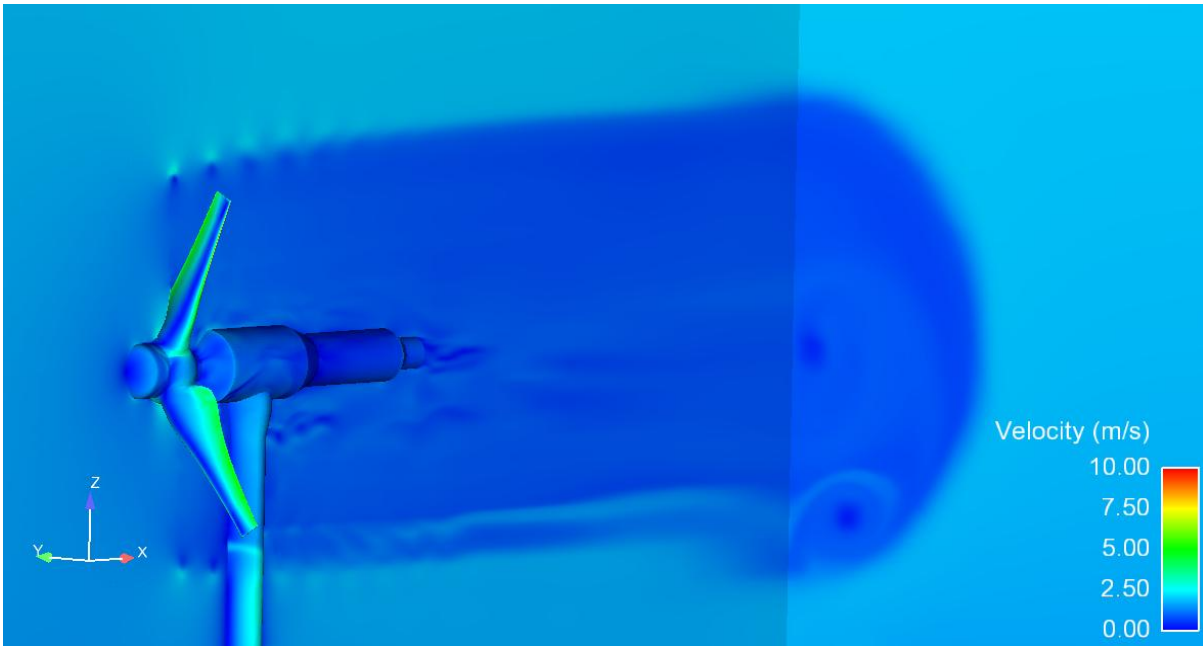
**Figure 13.** Detail of instantaneous velocity field obtained with LES.

Vortical motions are also visualised by plotting isosurfaces of streamwise vorticity, coloured by (instantaneous) Q Figure 14. Here, Q is defined by

$$Q = \frac{1}{2}(S_{ij}S_{ij} - \Omega_{ij}\Omega_{ij})$$

With this definition (the sign is often reversed in the literature) a negative Q signifies an excess of rotational over shear strains. All cases show an interaction between vorticity emanating from the blade tips with that shed behind the tower. Turbulence, particularly in Case 2, causes distortion and aids in the break-up of the vortex structures.
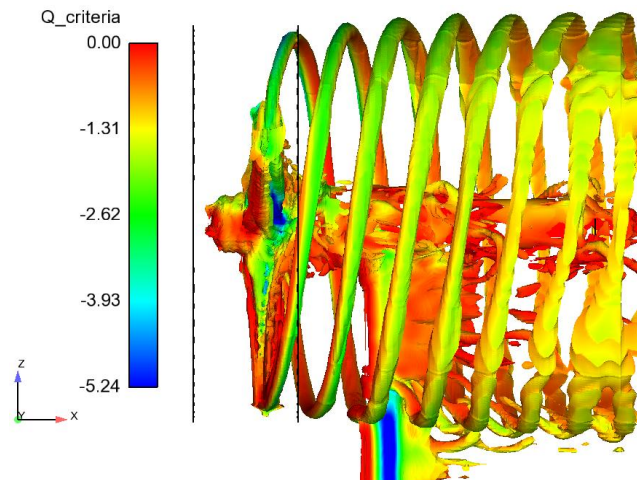
(a) Case 1: Zero-turbulence approach flow
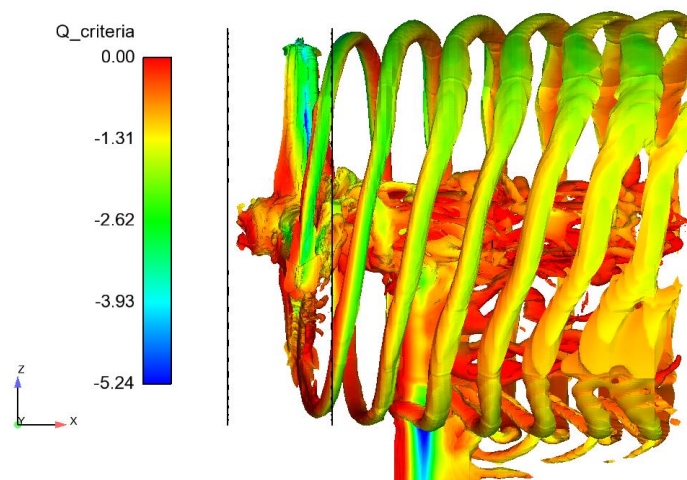
(b) Case 2: SEM inlet turbulence; inlet statistics from channel-flow simulation
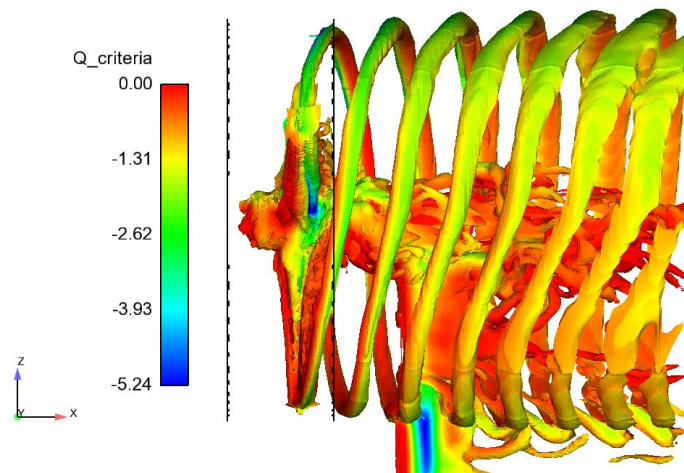
(c) Case 3: SEM inlet turbulence; length scales halved.

Figure 14. Iso-surfaces of streamwise vorticity, coloured by vorticity indicator Q.

4. COMPARISON WITH FIELD MEASUREMENTS

4.1 Available Data

Experimental data was supplied by the University of Edinburgh in Matlab (.mat) files, for onset flow-velocity data, and by Alstom in the form of ASCII comma-separated-value (.csv) files for turbine measurements, including loads and rotational speed. The flow data provided includes depth profiles of velocity measured from bed-mounted ADCPs, reference velocity from overlapping intervals of turbine data and processed values of length scales obtained from turbine-mounted instruments at mid-depth. The load data analysed for this study was of 3.5 hours duration during a single tide in October 2013. This dataset was selected on the basis of the number of occurrences of the target flow speed range of $1.7 - 1.9$ m s^{-1} to provide comparison with a nominal simulation flow speed of 1.8 m s^{-1}. The turbine operates with zero pitch throughout this dataset, providing a basis for direct comparison to the zero-pitch CFD. An average tip-speed ratio of 5.2 was identified to define the rotation rate used in the LES simulations with turbulent inflow.

Load Data
Data sampling was at 50 Hz. The following data was extracted from data file "2013-10-30 Slow Flood Tide Controller & Both SGs.csv".

Shaft data includes:
− rotation rate: this could be inferred from the stated shaft speed or by differentiating the blade angle; in this instance we have used the former.
− torque: recorded directly.

Blade data includes:
− flapwise and edgewise bending moments at 1.16 m and 2.71 m from blade root (2.45 m from rotor centre line, or $r/R = 0.272$).
By interpolation from the given blade geometry, the chord line (leading edge to trailing edge) is twisted 20.7º and 13.0º to the rotor plane at 1.16 m and 2.71 m respectively from the blade root fixing.

Velocity Data
Hub-height velocity reference data was extracted from Matlab data file "U_Ref.mat" and consists of 10 s moving averages from data sampled at 1 Hz. Note that this reference velocity corresponds to that at nacelle height (our U_{hub}), but at 2 diameters rather than 1 diameter upstream of the turbine rotor. The nacelle-height velocity is about 1% and 2.7% larger than the channel bulk velocity for flood profile and fully-developed channel flow respectively. Depth profiles of velocity and of some turbulence parameters have also been provided; these are similar to the onset profile employed (see Figure 6).

4.2 Comparison Between Simulations and Experiment

4.2.1 Load Coefficients

Figures 15 and 16 show the phase-averaged whole-rotor power and thrust coefficients (rotation angle $\theta = 0°$ corresponds to a nominated blade vertically upward), comparing experimental data with RANS simulations (SST k-ω turbulence model; low turbulence inflow) and LES. Experimental data indicates a power coefficient of about 0.43–0.44 (but sensitive to sampling interval on both power and velocity). For the LES we considered both zero approach-flow turbulence (Case 1) and more realistic inlet turbulence provided by SEM (Cases 2 and 3). In the LES calculations, averaging started after one complete pass-through and was phase-averaged over between 5 and 7 rotations, depending on case.
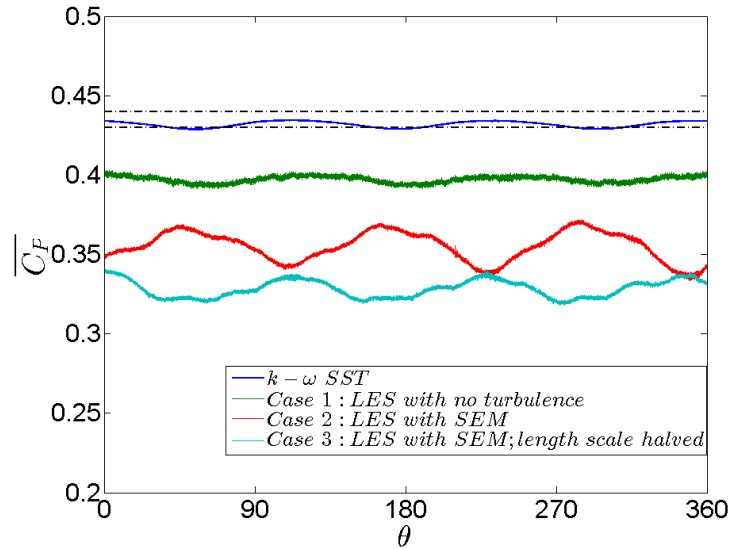
Figure 15. Phase-averaged power coefficient (whole-rotor); reference velocity is the hub-height velocity at inlet.
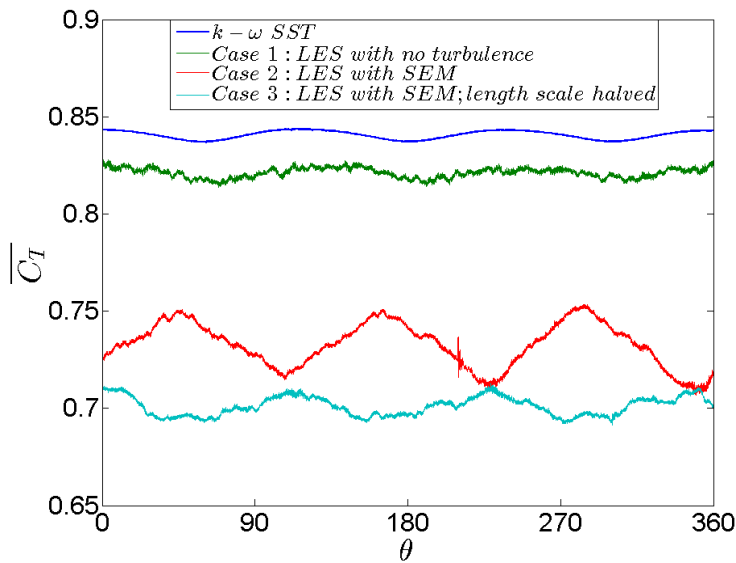
Figure 16. Phase-averaged thrust coefficient (whole-rotor); the reference velocity is the hub-height velocity at *inlet*.

In the low-turbulence cases, power coefficients with the RANS model (k-ω SST) are comparable with experiment, but LES values (Case 1) are slightly lower. A similar relationship between computational coefficients holds for thrust coefficient, but here we have no experimental data with which to compare.

Once turbulence is introduced at inlet by the SEM method (Case 2), the LES results in Figure 15 show a smaller power coefficient: the cycle average being about 0.36. This is due to the reference (hub-height) mean velocity directly upstream of the turbine being less than at the same height at inflow because of streamwise flow evolution. The turbine encounters a slightly smaller approach flow velocity, but the effect is amplified by the velocity-cubed dependence of power. As shown in Figure 17, the hub-height mean velocity varies most rapidly near inlet. This may result from a basic failure of the SEM method to capture sufficient statistics of the turbulent flow, the much higher Reynolds number in the present simulation than the channel flow on which the SEM statistics were based, a comparatively coarse grid, or a combination of all three effects. Beyond this near-inlet development region, however, the hub-height velocity remains relatively constant, at least to within one diameter of the turbine rotor. The velocity at this latter location may therefore be used as a more appropriate reference velocity to represent the approach flow.
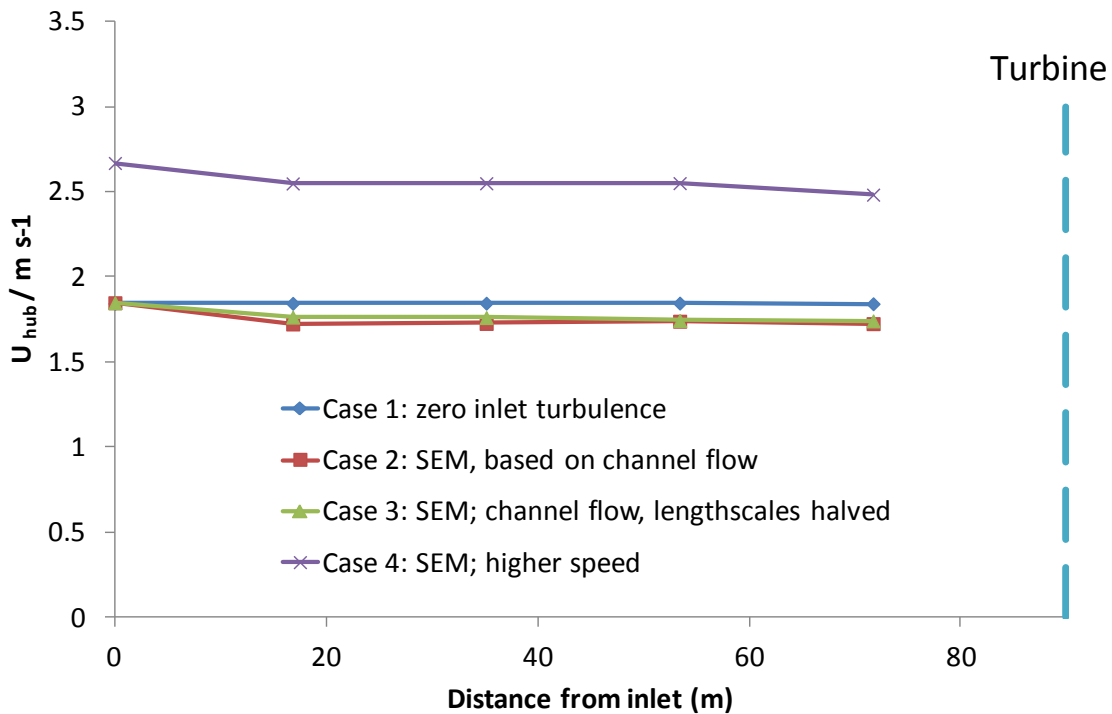

Figure 17. Variation of hub-height mean velocity with streamwise distance from inlet.

If the power and thrust coefficients are now normalised by the immediately-upstream hub-height velocity (taken, for convenience, as a spanwise average at one diameter upstream) then we obtain the revised coefficients shown in Figures 18 and 19. With this revised reference velocity the power coefficient from simulations with basic SEM (Case 2) agrees well with experiment, whilst the predictions using SEM with more realistic length scales (Case 3) is improved. Note that in the low-turbulence simulation (Case 1) the flood profile does not evolve significantly between inlet and turbine and no such adjustment is necessary. It is, however, unclear why C_P values are lower for LES than RANS simulations here, although it is noted that the RANS simulations were run with a lower mesh resolution and larger timestep (see Report for MD1.5).
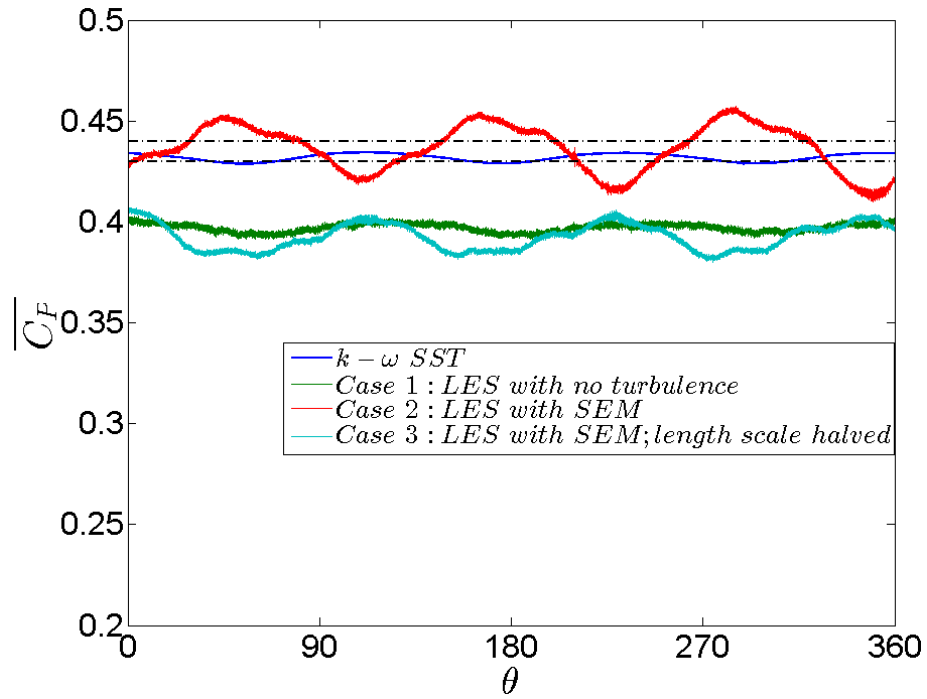
Figure 18. Phase-averaged power coefficient (whole-rotor); the reference velocity is the hub-height velocity one diameter upstream of the rotor.
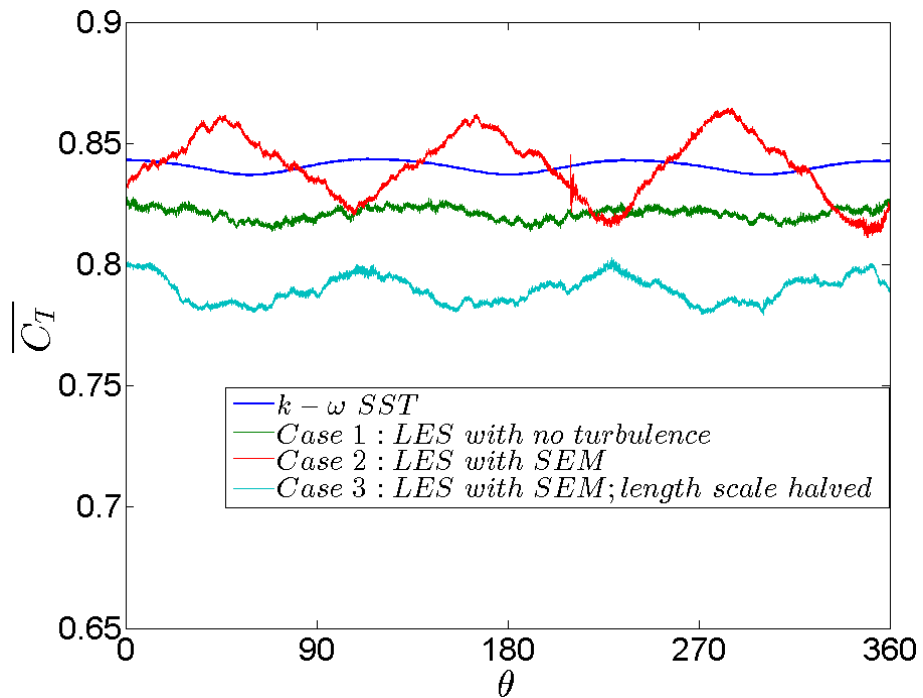

Figure 19. Phase-averaged thrust coefficient (whole-rotor); the reference velocity is the hub-height velocity one diameter upstream of the rotor.

The variations of power coefficient for the whole rotor over a cycle will be transmitted to the shaft, potentially causing variations in rotor speed that depend on the overall inertia. Low-turbulence approach-flow simulations by both RANS and LES show the characteristic signature of the three individual blades passing in front of the support tower, resulting in three minima of power per cycle.

Load coefficients have been computed also for the higher-speed calculation (Case 4: $U_b = 2.6$ m s^{-1}). Power coefficients, with reference velocity again determined one diameter upstream of the turbine, are shown in Figure 20.
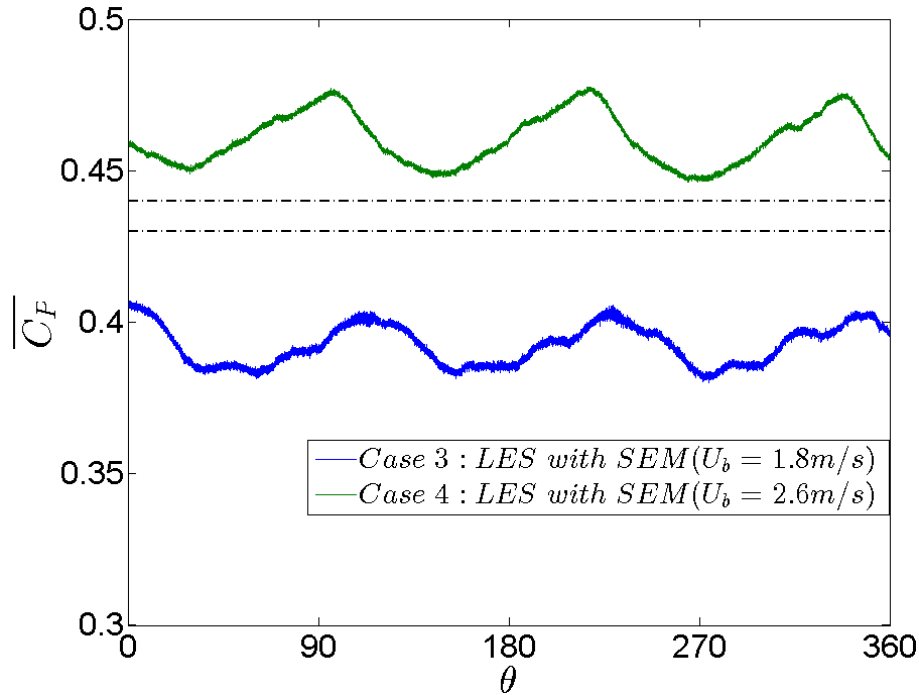

Figure 20. Phase-averaged power coefficient at different speeds (whole-rotor); the reference velocity is the hub-height velocity one diameter upstream of the rotor.

Further differences between RANS and LES simulations are examined by plotting the pressure coefficient on one blade at various radii. Pressure is normalized to the local azimuthal speed ΩR to provide comparable range over the blade radius (and circumvent the issue of approach-flow velocity). The negative pressure coefficient is plotted for clarity and to emphasise lift. Figure 21 shows the resultant c_p values based on average pressure over several cycles, whilst Figure 22 shows an instantaneous snapshot, illustrating the large time-varying fluctuations beyond about 50% chord and 50% tip radius that are resolved by LES, even without inflow turbulence (Case 1). Differences between average pressures using RANS and LES are relatively small, mainly being confined to the suction surface downstream of peak suction at radial distances between about $r/R = 0.4$ and 0.8.
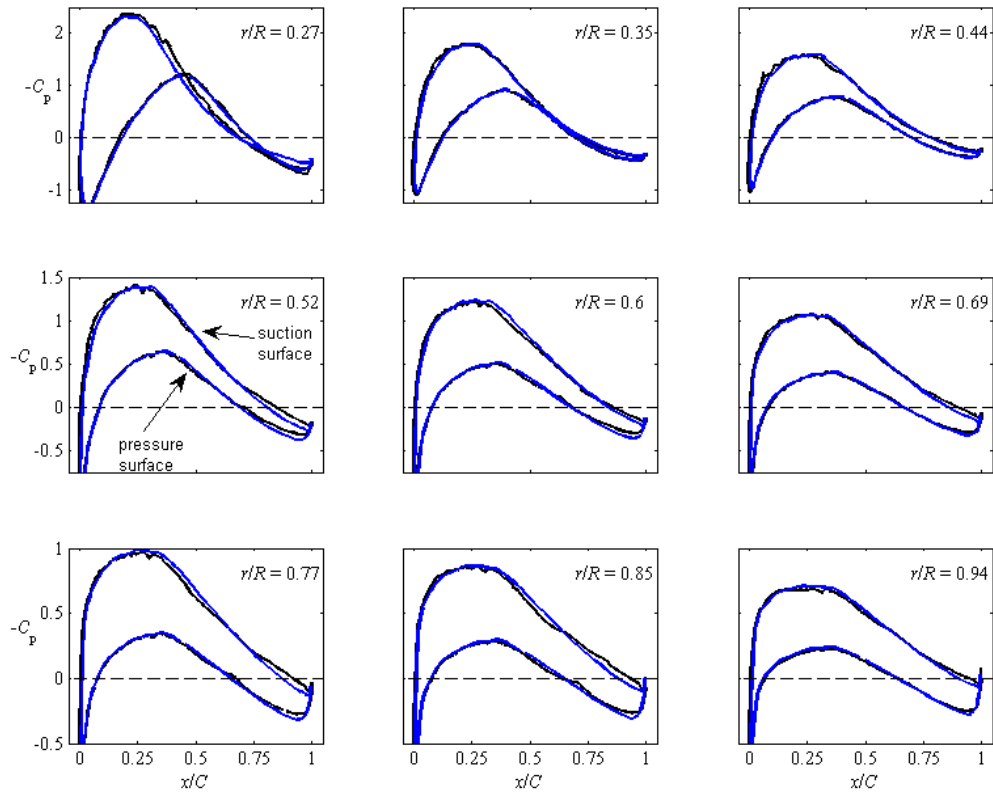
Figure 21. Average pressure-coefficient distributions at various radii; comparison of LES (black) and RANS k-ω SST (blue).
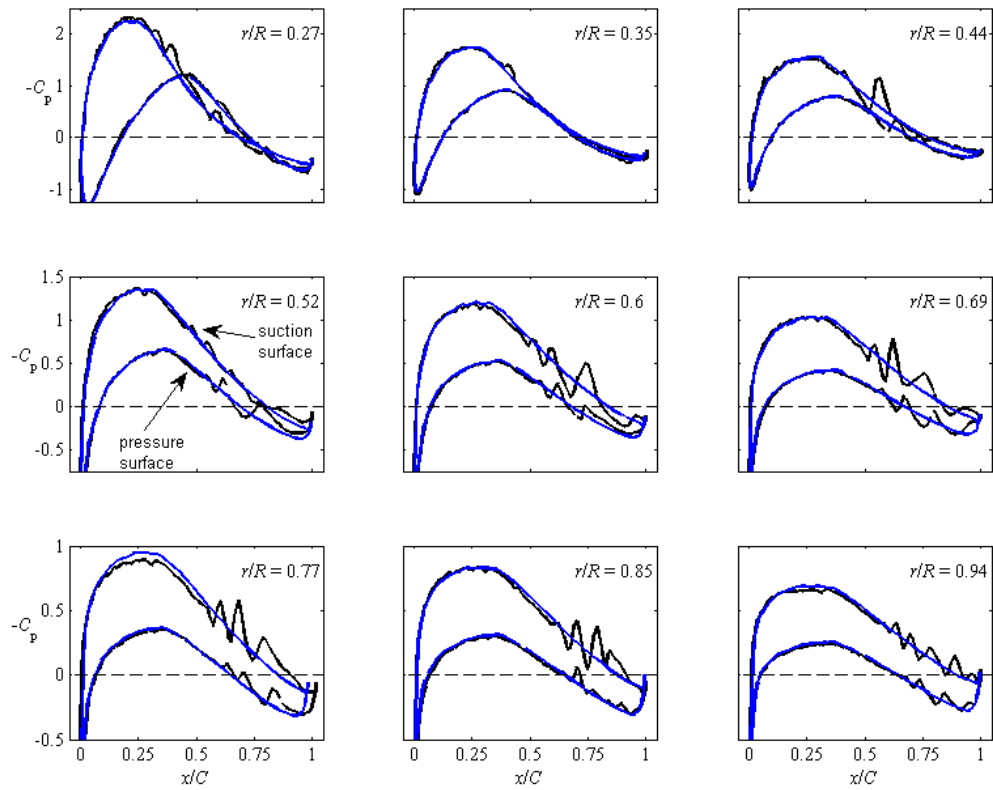

Figure 22. As Figure 21, but based on instantaneous pressure.

Strong evidence of the effect of onset turbulence on the cyclical loads for an individual blade is shown in Figure 23, which presents detail of the time-varying power on a single blade, divided by the average for the whole rotor. (For CFD, with fixed rotor speed, this ratio would be the same for torque as power; however, the experimental data was gathered at varying rotor speed, so that direct comparison on torque is more appropriate) Whereas the low-turbulence results for RANS and LES are very similar, with phase-averaged variations of about ±10% around the cycle average of 0.333, substantially greater variations are observed with approach-flow turbulence. Note that this graph presents a conservative, phase-averaged (over about 10 cycles) picture of the variation in power. Figure 24 shows variations within one cycle: variation from one cycle to another is even greater, as shown in Section 4.2.2 for blade bending moment.
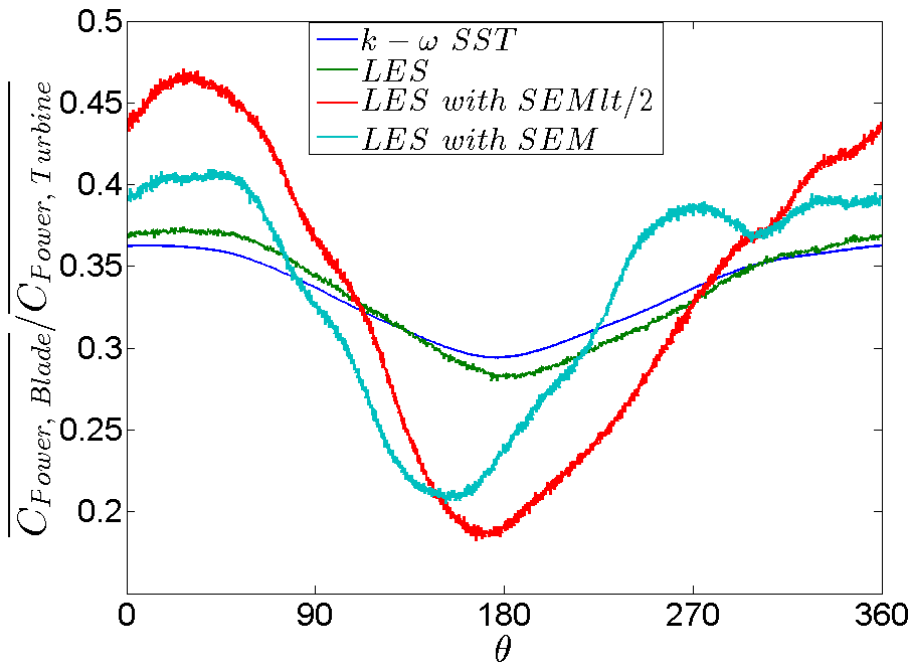

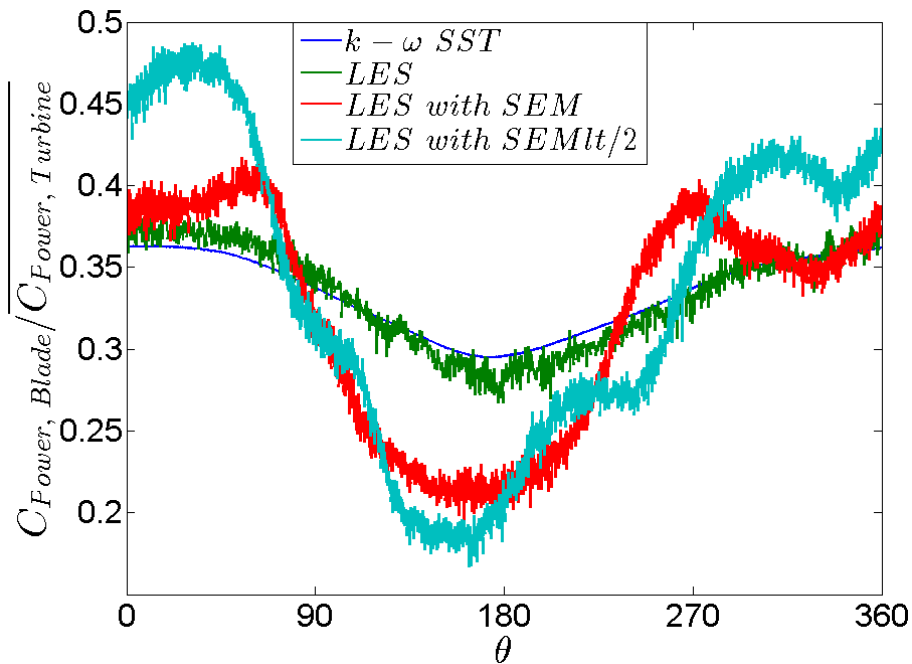**Figure 23.** Phase-averaged power coefficient (single blade, normalised by average for whole rotor).

Figure 24. Variation of instantaneous load coefficients in the course of a single rotation.

4.2.2 Blade Bending Moments and Spectra

Figure 25(a) shows experimental measurements of flapwise bending moment where the 10-minute approach flow velocity (1.76 m s^{-1}) is close to that simulated by LES (1.8 m s^{-1}). This shows considerable variation from one cycle to another. Figure 25(b) shows the plot restricted to cycles where the 30 s average of the reference velocity is within 0.05 m s^{-1} of the LES; it is also normalised by the mean of its individual cycle. Using the phase-averaged mean and standard deviation from the latter, experimental and LES results for flapwise bending moment (at 1.16 m from blade root; $r/R = 0.272$) are shown in Figure 26.
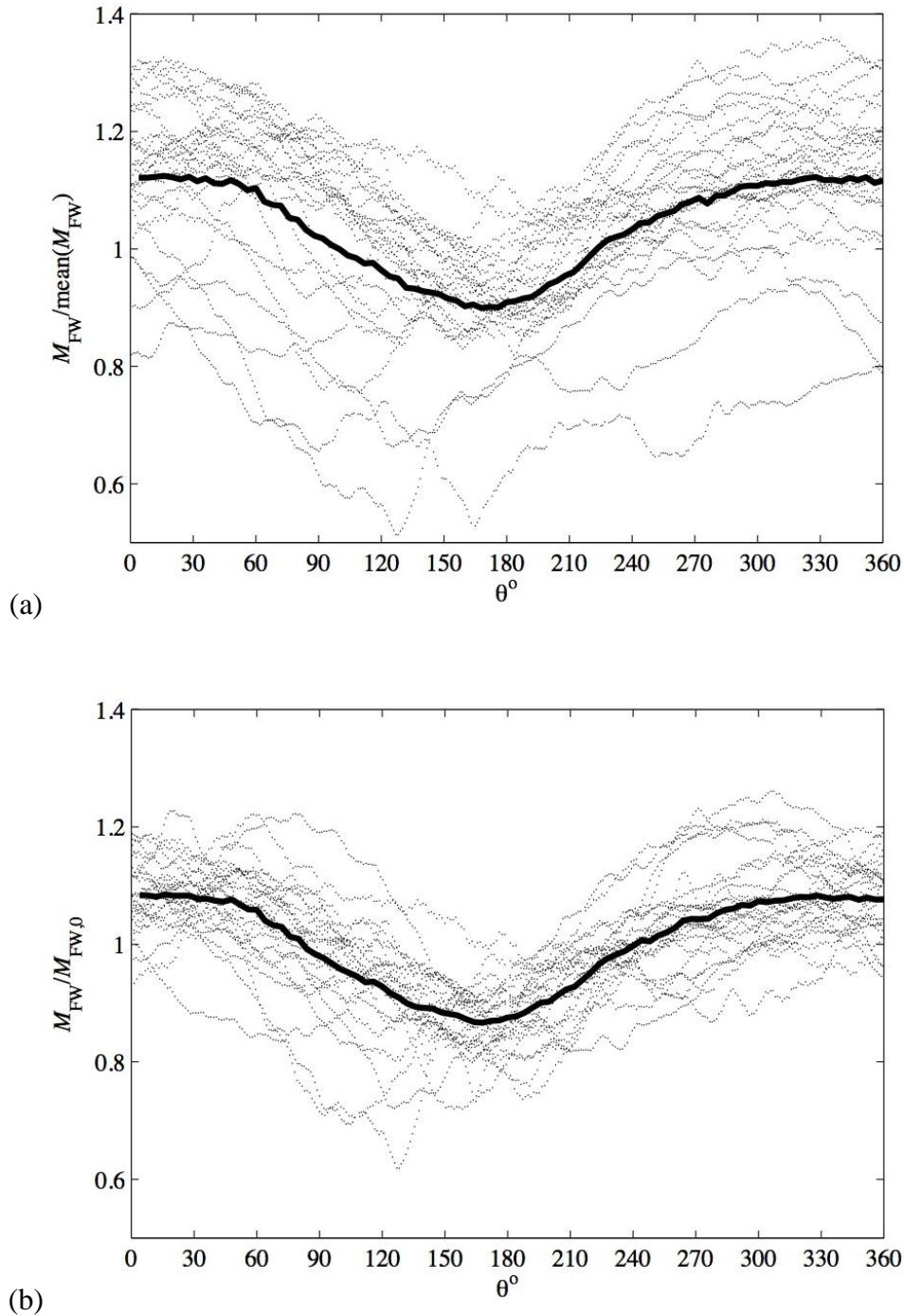

(a)

(b)

Figure 25. Variation of flapwise (FW) bending at $r/R = 0.272$ with blade position (θ) during a 10-minute sample with $U_{ref} = 1.76 \text{ m s}^{-1}$; (a) all data; (b) only cycles where the 30 s average U_{ref} is in the range 1.75 to 1.85 m s^{-1}; phase average (solid) is also shown.

(For a constant-speed rotor) fluctuations in load coefficients on a single blade have a number of sources:

- tower-passing (and velocity-shear) frequency $f_0 = 1/T_0$, where T_0 is the period of a single rotation; (note that the whole rotor, with three blades, will exhibit key frequency $3f_0$);
- blade-generated turbulence;
- approach-flow turbulence.

Numerically (or experimentally), fluctuations can be resolved up to the Nyquist frequency $f_{max} = 1/(2\Delta t)$.

Figure 26 indicates that the turbine blades are not the source of fluctuations in bending moment, as with zero-inlet-turbulence LES (Case 1) there is negligible variation in flapwise bending moment. A similar result (not shown) is obtained with k-ω SST. Turbulent inflow increases both phase-averaged fluctuations (solid lines) and between-cycle variation (shaded regions). Due to the small number of rotations that we have been able to simulate with LES, phase-averaged variation is not fully developed (hence the "wiggles") and the intra-cycle variation (width of the shaded region) is mainly under-predicted.
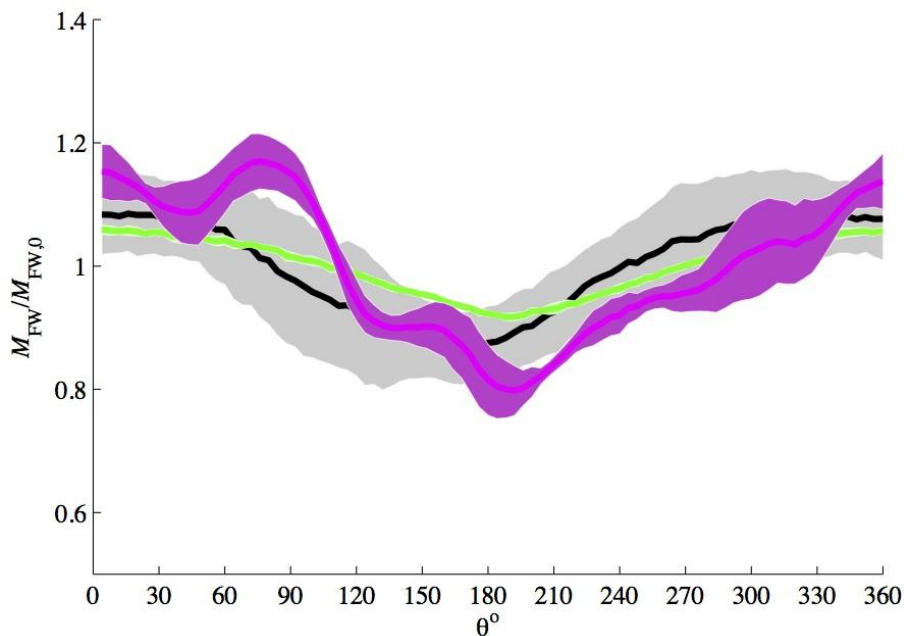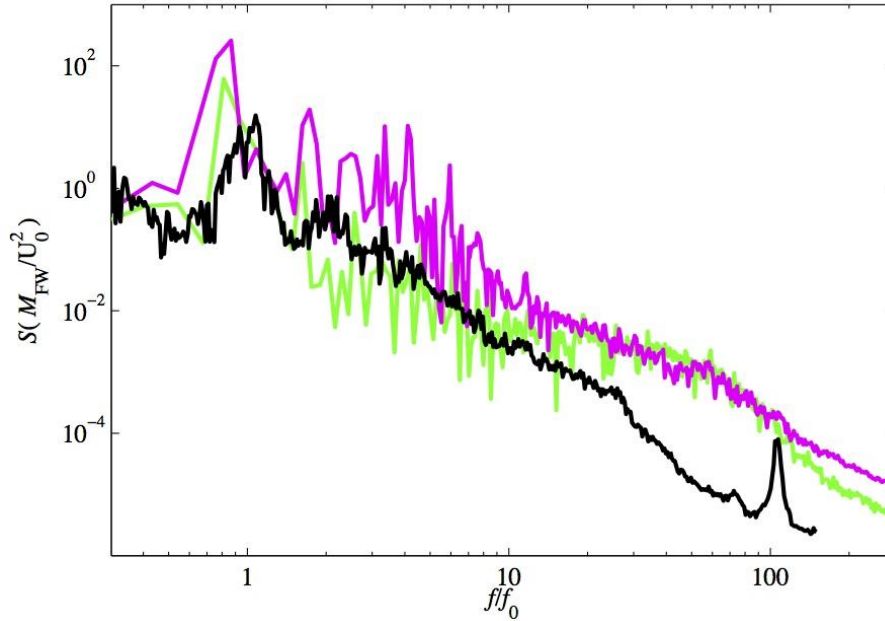

Figure 26. Variation of flapwise bending moment for a single blade: experiment (black/grey); LES with no turbulence at inflow, Case 1 (green); LES with SEM inflow, Case 4 (purple); variation by one standard deviation either side is shaded.

Figure 27(a) shows the power spectrum of the flapwise bending moment on a specific blade. The spectral density is plotted against f / f_0, where f_0 is the primary tower-passing frequency. (This abscissa allows comparison of cases with different rotation speeds on the same axes.) Experimental data shown here was taken (at 50 Hz) from one 10-minute sampling period where the average flow speed was 1.76 m s^{-1}. LES data is plotted for no inflow turbulence (Case 1) and for the higher-speed case with inflow turbulence (Case 4): the absence of energy in the 3–$20f_0$ range when there is no inflow turbulence is evident in the plot.

Experiment and computation differ largely because of the lower total variance in flapwise bending moment in the CFD (as a result of the fewer cycles available to sample). Relative amounts of energy at

different frequencies are shown in Figure 27(b), where the power spectrum has been normalised by the overall energy. The CFD spectra are more "peaky", a consequence of the relatively small number of cycles simulated, but the largest harmonics and decay rate of the power spectrum ($f > 20f_0$ for zero turbulence – Case 1 and $f > 3f_0$ with onset turbulence – Case 4) are well predicted in the LES simulations.

(a) Unnormalised spectrum

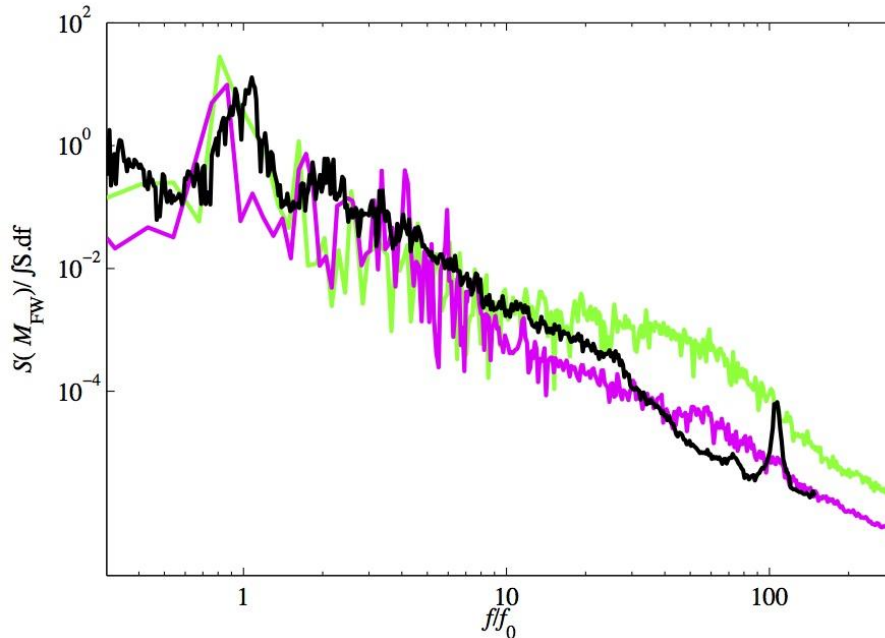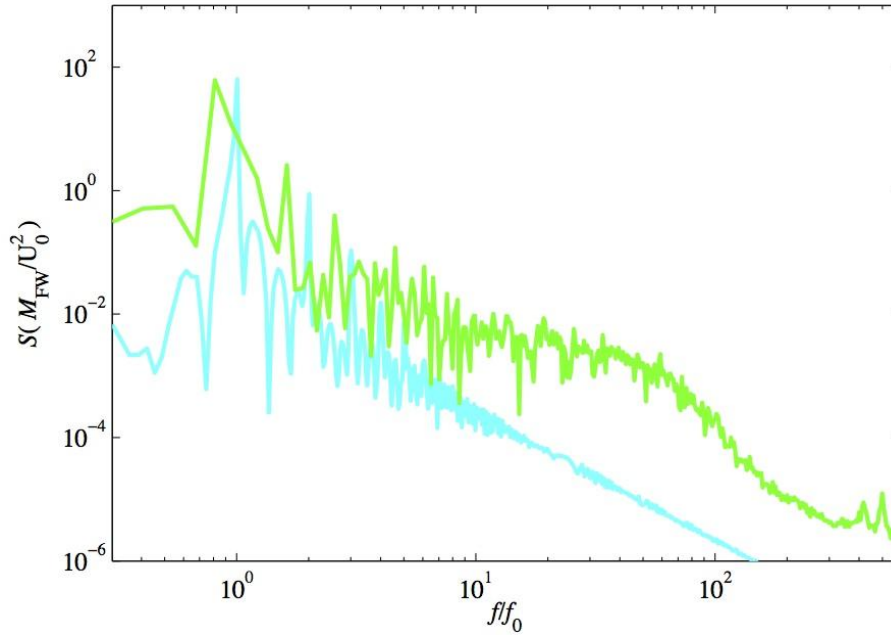(b) Normalised by total variance

Figure 27. Spectrum of flapwise bending moment at $r/R = 0.272$: experiment (black), LES with no inflow turbulence, Case 1 (green) and LES with turbulent inflow, Case 4 (purple).

Figure 28 compares spectra for RANS and LES closures. The former is not individual-eddy-resolving, so lacks the energy in the higher frequencies associated with blade-generated turbulence (see also Figure 22).

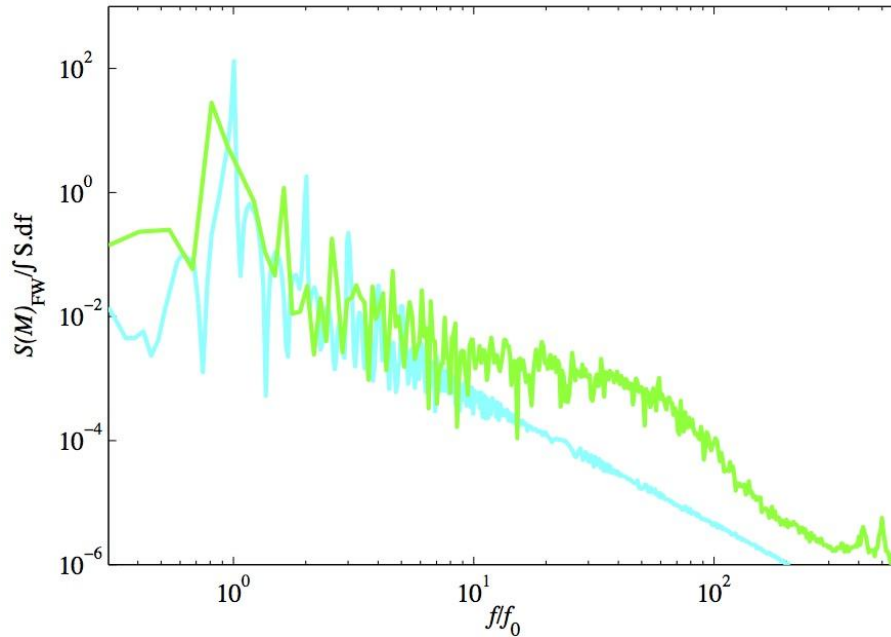(a) Unnormalised spectrum

(b) Normalised by total variance

Figure 28. Spectrum of flapwise bending moment, comparing RANS (cyan) and LES (green) closures, both with no turbulence at inflow.

Finally, Figure 29 shows the normalised power spectra of the three LES simulations (Cases 2, 3, 4) with inflow turbulence implemented using SEM using different factors applied to length scales and Reynolds stresses. The figure suggests that, once normalised by the total variance, the spectra collapse onto a single curve. However, the spikiness of the graph in the energy-bearing frequencies is an indication of the relatively low number of turbine cycles that it has been computationally-practical to date to simulate with LES.
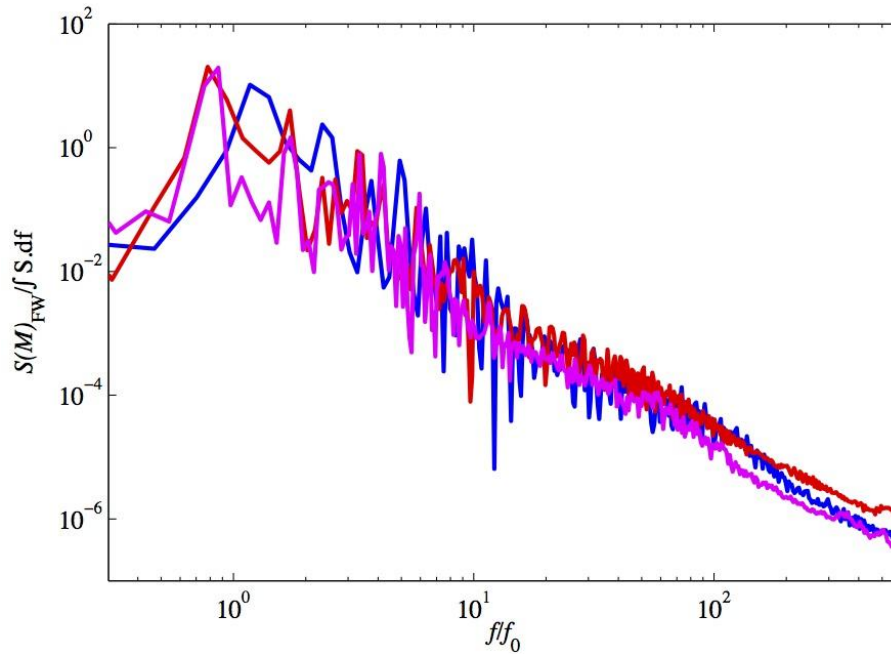

Figure 29. Normalised power spectrum of flapwise bending moment, comparing the LES cases with inflow turbulence: Case 2, $U_b = 1.8$ m s^{-1} (blue); Case 3, $U_b = 1.8$ m s^{-1}, length scales halved (red); Case 4, $U_b = 2.6$ m s^{-1} (purple).

5. CONCLUSIONS AND FURTHER WORK

LES calculations have been performed, with and without inflow turbulence, and compared with RANS calculations and experimental data.

To compare directly with experiment, power coefficients are now based on the hub-height mean velocity at one diameter upstream of the rotor plane. In the low-turbulence inlet cases RANS calculations give mean C_P values of about 0.43 and LES values of about 0.40, the value fluctuating slightly within a cycle because of support-tower influence and inflow velocity shear.

For cases with inflow turbulence there is considerable flow development between inlet and turbine rotor (for both RANS and LES). For LES it is unclear whether this is an intrinsic feature of the SEM technique that has been used to synthesise turbulence (because this supplies only first and second moments of the velocity field, with a crude measure of correlation/eddy size), the fact that the supplied statistics came from a channel-flow calculation at a much lower Reynolds number, or that the turbine simulation is on a much coarser grid. Because of the flow development upstream of the turbine it is vital to use the velocity immediately upstream of the turbine as a reference velocity, rather than that nominally specified on the inlet plane. When power coefficients are renormalised to the hub-height velocity one diameter upstream, C_P values are much more in line with RANS and experiment, although inflow turbulence amplifies both instantaneous and phase-averaged load fluctuations within a cycle.

Spectral analysis of the fluctuating blade-bending moments emphasise that an LES approach with appropriate inflow turbulence is necessary to capture the correct spread of energies at all frequencies. Non-eddy-resolving closures (RANS) lack the higher-frequency range associated with blade-generated turbulence, whilst the relatively high energies at mid-range frequencies (from about 3 to 20 times the main rotational frequency) require that inflow turbulence be simulated. At lower frequencies the loading is largely dependent on the shear profile and the tower. Overall variance is not well-simulated, in part because the computational demands of LES limit the number of rotations simulated to date. However, once normalised by the total variance, all LES calculations with synthetic inflow turbulence show spectral decay rates in good agreement with experimental data.

For the Future

The work reported here threw up many challenges. Although LES with inflow turbulence is the only method available that is capable of capturing realistic fluctuations in load over a wide frequency range, it comes at a considerable computational cost. Even with massive parallelisation a single rotation takes about 6 days to compute, and a minimum of 10 rotations would be required for reasonable averages and spectra. In the longer term, particular numerical improvements to *Code_Saturne* could be made to ameliorate this:
- a residuals-based convergence criterion to adapt the number of inner iterations per timestep;
- second-order timestepping working with LES, allowing a larger timestep to be used;
- pressure-velocity coupling to be completely independent of timestep.

Specification of inflow turbulence and its effect on flow development remains a problem. Synthetic eddy modelling is an active field of research. More work is necessary to understand whether the flow development is primarily due to the supplied statistical input or the intrinsic method of generating eddies. In the latter case, an active field of research is divergence-free SEM (Poletto et al., 2011), where eddies are specified by vorticity rather than their velocity field. However, as reported in MD1.5, this does not yet show compelling evidence of improved performance over the current method.

APPENDIX: SUMMARY OF EARLIER MD1 REPORTS

MD1.1

The key developments in MD1.1 were:
- development of our own sliding-interface method to deal with rotating elements;
- construction of a computational model of a laboratory turbine (rotating parts only) of Bahaj et al. 2007a,b (the "Southampton turbine") using Fluent's Gambit grid-generation software.

We were forced to develop our own sliding-interface method after experiments with the suggested method in Code_Saturne (having two instances of the code working for separate domains and communicating at regular intervals) proved unworkable. An alternative approach – working in a rotating reference frame, with applied Coriolis forces – was available for validation, but could not be used for full geometry representation because of the necessity of including the stationary support tower, sea bed and free surface.

At this stage the sliding-mesh interface method was being validated (several simple-geometry cases including cylinder and cube were included) and still needed parallelisation. Initial (laminar-flow) calculations with the turbine demonstrated feasibility only.

MD1.2

The key developments in MD1.2 were:
- full description of the sliding-interface method, including implementation and validation;
- extension of the Southampton-turbine computational model to include support tower;
- RANS and LES calculations of the Southampton turbine, including comparison with experimental data and a parametric study of its response to different turbulence levels.

Various RANS turbulence models were investigated, with the SST k-ω model found to produce significant improvement in prediction of mean rotor loads over the standard k-ε model. Only LES was found to match the mean rotor-load characteristics for significantly off-design tip-speed ratios. This also provided a preliminary assessment of the influence of inflow turbulence generated by SEM on the unsteady rotor loads, but at considerable computational cost.

Two journal papers (McNaughton et al., 2014 and Afgan et al., 2013) were published as a result of this work, as well as conference papers in the EWTEC, AWTEC and THMT series.

MD1.3

The key developments in MD1.3 were:
- summary of the ALE (moving-mesh) method in *Code_Saturne* and testing of moving-free-surface routines to simulate waves;
- significant improvements to the parallelisation of the sliding-mesh interface method;
- construction of a computational model of the Alstom turbine using the ICEM-CFD package.

Free-surface movement was validated successfully against theoretical solitary-wave profiles, small-amplitude regular waves and waves passing over a cylinder. For waves without currents (and hence no well-defined inflow boundary) there remains an outstanding issue with inflow/outflow boundary conditions which could lead to a gradual loss of fluid from the domain, but this is not directly applicable to the current-driven turbine case.

Initial testing was performed with the Alstom turbine model, including (as we were awaiting flow data) uniform approach flow. Some testing of a single wave passing over the turbine was performed, but it was realised that computation times for a series of waves would be prohibitive.

MD1.5 (Out of sequence due to amendments to the MD1.4 milestones)

The key developments in MD1.5 were:
- full RANS simulation of the 1MW Alstom turbine (with idealised support structure) at a fixed rotation rate, including mean-flow velocity shear with realistic ebb and flood profiles based on measurements at the EMEC test site;
- high-resolution channel-flow calculations to characterise the depth profile of mean velocity, Reynolds stresses and length scales in fully-developed flow;
- assessment of the performance of synthetic-eddy methods (SEM) for providing inflow conditions for future LES simulations of the Alstom turbine.

RANS simulations (with the k-ω SST model) investigated the effects of upstream velocity shear and identified fluctuations in blade loading due to this and the effects of the support tower. However, significant levels of upstream turbulence were found to diffuse the prescribed velocity profiles before they reached the rotor.

Different variants of the SEM approach were investigated, and a sequence of fully-developed channel-flow simulations were performed, the object being to define suitable profiles of Reynolds stresses and integral length scales as inputs to the LES simulations of the Alstom turbine in MD1.4.

MD1.4 (This Report)

Major elements:
- LES modelling of the Alstom turbine;
- prediction of fluctuating blade loads under realistic turbulence conditions;
- comparison with experimental data from the EMEC test site.

Publications Arising From This Project

Journals

Afgan, I., McNaughton, J., Apsley, D., Rolfo, S., Stallard, T. and Stansby, P.K. (2013). Turbulent flow and loading on a tidal stream turbine by LES and RANS. International Journal of Heat and Fluid Flow 43, 96-108.

McNaughton, J., Afgan, I., Apsley, D.D., Rolfo, S., Stallard, T. and Stansby, P.K. (2014). A simple sliding-mesh interface procedure and its application to the CFD simulation of a tidal-stream turbine. International Journal for Numerical Methods in Fluids 74, 250-269.

Conferences

McNaughton, J., Rolfo, S., Apsley, D.D., Stallard, T. and Stansby, P.K., 2013, CFD power and load prediction on a 1MW tidal stream turbine with typical velocity profiles from the EMEC Test Site, 10th European Wave and Tidal Energy Conference (EWTEC), Aalborg, Denmark.

McNaughton, J., Rolfo, S., Apsley, D., Stansby, P.K. and Stallard, T., 2012, CFD prediction of turbulent flow on an experimental tidal-stream turbine using RANS modelling, 1st Asian Wave and Tidal Energy Conference (AWTEC), Korea.

Afgan, I., McNaughton, J., Apsley, D., Rolfo, S., Stallard, T. and Stansby, P.K., 2012, Large-eddy simulation of a 3-bladed horizontal-axis tidal stream turbine: comparisons to RANS and experiments, Turbulence, Heat and Mass Transfer 7 (THMT7), Sicily.

The work was also reported at two workshops on tidal energy at the University of Oxford and at a workshop of the UK turbulence consortium.

Theses

McNaughton, J. (2013). Turbulence modelling in the near field of an axial flow turbine using *Code_Saturne*, PhD Thesis, University of Manchester.

REFERENCES

Afgan, I., McNaughton, J., Apsley, D., Rolfo, S., Stallard, T. and Stansby, P.K. (2013). Turbulent flow and loading on a tidal stream turbine by LES and RANS. International Journal of Heat and Fluid Flow 43, 96-108.

Bahaj, A.S., Batten, W.M.J. and McCann, G., 2007a, "Experimental verifications of numerical predictions for the hydrodynamic performance of horizontal axis marine current turbines", Renewable Energy, 32, 2479–2490.

Bahaj, A.S., Molland, A.F., Chaplin, J.R. and Batten, W.M.J., 2007b, "Power and thrust measurements of marine current turbines under various hydrodynamic flow conditions in a cavitation tunnel and a towing tank", Renewable Energy, 32, 407–426.

Germano, M., Piomelli, U., Moin, P. and Cabot, W.H. (1991). A dynamic subgridscale eddy viscosity model. Physics of Fluids A: Fluid Dynamics 3, 1760 – 1765.

Jarrin, N., Prosser, R., Uribe, J., Benhamadouche, S. and Laurence, D. (2009). Reconstruction of turbulent fluctuations for hybrid RANS/LES simulations using a synthetic-eddy method. International Journal of Heat and Fluid Flow 30(3), 435 – 442.

Lilly, D.K. (1992). A proposed modification of the Germano subgridscale closure method. Physics of Fluids A: Fluid Dynamics 4, 633 – 635.

McNaughton, J., Afgan, I., Apsley, D.D., Rolfo, S., Stallard, T. and Stansby, P.K. (2014). A simple sliding-mesh interface procedure and its application to the CFD simulation of a tidal-stream turbine. International Journal for Numerical Methods in Fluids 74, 250-269.

McNaughton, J. (2013). Turbulence modelling in the near field of an axial flow turbine using *Code_Saturne*, PhD Thesis, University of Manchester.

Poletto, R., Revell, A., Craft, T. and Jarrin, N. (2011). Divergence-free synthetic-eddy method for embedded LES inflow boundary conditions. In: Seventh International Symposium On Turbulence and Shear Flow Phenomena (TSFP-7), Ottawa.